AIP | Physics of Fluids

On the relative rotational motion between rigid fibers and fluid in turbulent channel flow

C. Marchioli, L. Zhao, and H. I. Andersson

Citation: Physics of Fluids **28**, 013301 (2016); doi: 10.1063/1.4937757
View online: http://dx.doi.org/10.1063/1.4937757
View Table of Contents: http://scitation.aip.org/content/aip/journal/pof2/28/1?ver=pdfcov
Published by the AIP Publishing

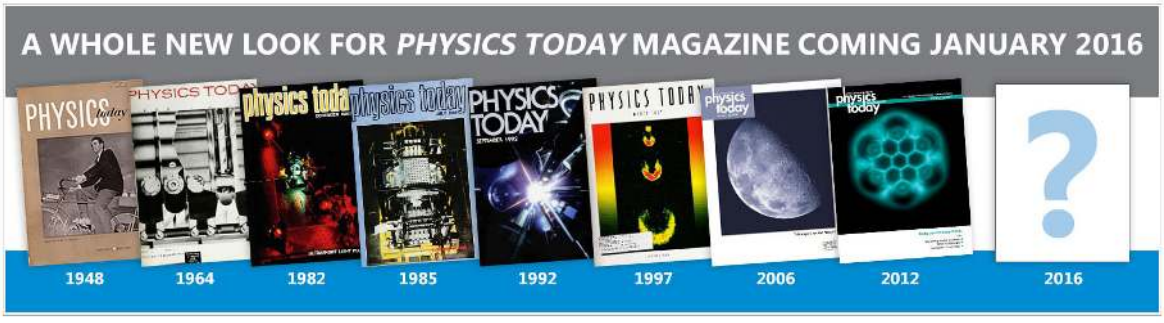

On the relative rotational motion between rigid fibers and fluid in turbulent channel flow

C. Marchioli,[1] L. Zhao,[2,a)] and H. I. Andersson[1,2]
[1]*Department of Electrical, Management and Mechanical Engineering, University of Udine, 33100 Udine, Italy*
[2]*Department of Energy and Process Engineering, Norwegian University of Science and Technology, 7491 Trondheim, Norway*

(Received 29 May 2015; accepted 1 December 2015; published online 5 January 2016)

In this study, the rotation of small rigid fibers relative to the surrounding fluid in wall-bounded turbulence is examined by means of direct numerical simulations coupled with Lagrangian tracking. Statistics of the relative (fiber-to-fluid) angular velocity, referred to as slip spin in the present study, are evaluated by modelling fibers as prolate spheroidal particles with Stokes number, St, ranging from 1 to 100 and aspect ratio, λ, ranging from 3 to 50. Results are compared one-to-one with those obtained for spherical particles ($\lambda = 1$) to highlight effects due to fiber length. The statistical moments of the slip spin show that differences in the rotation rate of fibers and fluid are influenced by inertia, but depend strongly also on fiber length: Departures from the spherical shape, even when small, are associated with an increase of rotational inertia and prevent fibers from passively following the surrounding fluid. An increase of fiber length, in addition, decouples the rotational dynamics of a fiber from its translational dynamics suggesting that the two motions can be modelled independently only for long enough fibers (e.g., for aspect ratios of order ten or higher in the present simulations). © *2016 AIP Publishing LLC.* [http://dx.doi.org/10.1063/1.4937757]

I. INTRODUCTION

The rotational dynamics of elongated fibers in turbulent fluid flow is known to play a crucial role in a wide variety of industrial processes. Examples relevant to the present study include pulp and papermaking (see the works of Kvick *et al.*[1] and Lundell *et al.*[2] among others), borehole-cleaning operations in the oil and gas industry, which can be improved using fiber-based sweep fluids,[3] or injection molding of fiber-reinforced composites, commonly used in automotive applications.[4] In all these processes, the mechanical, thermal, and electrical properties of the final fiber composite depend not only on the spatial distribution of fibers but also, if not primarily, on their orientation within the flow. Fiber orientation is in turn correlated to the specific features of turbulence, namely, mean shear, local velocity gradients, and flow inhomogeneities. As demonstrated by recent studies (see for instance, the works of Ni *et al.*,[5] Challabotla *et al.*,[6] Gustavsson *et al.*,[7] Marchioli and Soldati,[8] Parsa *et al.*,[9] and Shin and Koch[10]), the strength of this correlation is strongly influenced by fiber anisotropy through fiber length, which adds to fiber inertia and flow anisotropy (in the case of wall-bounded flows) to deviate fiber rotation rates from those of spherical particles. In spite of all these studies, an aspect that remains little explored is how fibers rotate relative to the spin of the surrounding fluid, which is produced by the Lagrangian fluid velocity gradients (seen by the fiber along its trajectory). A first investigation on this problem was made by Ni *et al.*[5] and Marcus *et al.*[11] by means of simultaneous measurements of the orientation of rod-shaped particles and of the Lagrangian velocity gradients in homogeneous isotropic turbulence. These measurements

a)lihao.zhao@ntnu.no

allow a complete description of how the rod tumbling rate depends on the velocity gradients, showing an equally important contribution from vorticity and strain rate. A similar analysis, yet for tri-axial ellipsoidal particles, was conducted numerically by Chevillard and Meneveau.[12] These authors quantified the statistical dependence of particle orientations from the velocity gradient tensor and showed that predictions based on the assumption of a Gaussian process for the velocity gradient tensor provide unrealistic preferred vorticity-strain-rate tensor alignments. Currently, however, there are no such investigations for fibers within the dissipative subrange in inhomogeneous anisotropic turbulence.

From a modelling perspective, fiber rotation is a crucial variable for predicting the rheology of fiber suspensions: Rotation controls orientation, which in turn determines the additional non-Newtonian stress resulting from fiber injection within the Newtonian carrier fluid. In rheological models, fiber orientation is most often obtained from an ensemble-averaged evolution equation for the second moment of the orientation distribution[13–20] that requires closure relations for the fourth order moment of such distribution as well as proper expressions for the translational and rotational diffusion coefficients (see, e.g., Refs. 16 and 17). Typically, such expressions can be derived based on simplifying assumptions, e.g., two-dimensional fiber orientation (rather than three-dimensional as in real flow instances) and isotropic rotational diffusivity, which lead inevitably to discrepancies when assessed against experimental measurements.[17] Only recently, fiber-level simulations have been carried out to study the rotational diffusion of non-Brownian neutrally buoyant rigid fibers in a Newtonian fluid:[21] One purpose was to incorporate anisotropic diffusion in the second order evolution equation for the orientation tensor via a suitable closure approximation. Unfortunately, the resulting model yields unphysical behaviour at low fiber concentration, which is precisely the condition targeted in the present study. Other attempts to obtain the translational and rotational dispersion coefficients for fibers in turbulent flow (see the works of Olson[22] and Olson and Kekeres[23] among others) assumed negligible relative velocity between fibers and fluid. This assumption, which proved to be reasonable in simplified settings (e.g., isolated inertialess fiber moving in a stochastic turbulent velocity field as in Ref. 22 or in axisymmetric random flow as in Ref. 24), is not verified by the translational relative velocity for the case of inertial fibers in anisotropic turbulence, as shown recently by Zhao *et al*.[25] In fact, fibers are known to lead the fluid in the near-wall region, whereas they lag behind the fluid away from solid boundaries.[25] In the following, we will demonstrate that the assumption of negligible relative motion does not apply to the rotational relative velocity either, this being computed as deviation of the fiber rotation rate from the fluid rotation rate (and referred to as slip spin hereinafter).

This brief literature survey demonstrates that advancements in the physical understanding of fiber rotational dynamics in complex turbulent flows are needed to clarify the phenomenology of fiber motion and, therefore, to extend current modelling capabilities to more realistic configurations, in particular wall-bounded flows. In our opinion, one way to pursue this objective is to examine in detail the slip spin, namely, the rotation of individual fibers relative to the rotation of the surrounding fluid. As we will show in the following, this observable allows interesting physical insights into the dynamics of rigid fibers when these are exposed not only to fluctuating velocity gradients but also to strong mean shear (as occurs in channel and pipe flow). In addition, model development can benefit from the availability of numerical datasets that can complement existing experimental measurements. The slip spin is also an essential suspension variable in micro-continuum fluid mechanics, notably in the micropolar fluid theory introduced by Eringen.[26] A micropolar fluid is defined as a simplified subclass of microfluids[27] that exhibits both microrotational effects and microrotational inertia. A micropolar fluid is thus a constitutive model for a suspension containing rigid microstructures such as bar-like elements, polymeric additives, or blood cells. The rheological model for a micropolar fluid is expressed in terms of a microrotation viscosity μ_r and a microrotation vector field ω. The latter is associated with the angular velocity of the microstructures and has to be obtained from a separate differential equation for angular momentum. A recent analysis by Andersson and Zhao[28] showed that the contribution of spherical microstructures to the stress tensor of the suspension is proportional to the slip spin with the proportionality constant being μ_r.

In this paper, we thus examine the slip spin of fibers in turbulent channel flow, focusing on the effect of elongation (fiber length) upon fiber-fluid relative rotation. To this aim, results for fibers

are compared to those obtained for spherical particles with the same translational inertia. Because of the specific model adopted to represent the fibers (based on lumped-parameter fiber properties concentrated at the center of mass, as described in detail in Sec. II of this paper), we limit ourselves to small fibers, whose length is smaller than, or at least comparable to, the dissipative length scale of turbulence. In this limit, the fluid velocity variations across the fiber length are roughly linear and hence velocity gradients are constant and can be taken at the fiber center of mass. Shape and length effects on particle rotation have been examined in a number of previous studies (see the works of Byron *et al.*,[29] van Wachem *et al.*,[30] Abbasi-Hoseini *et al.*,[31] Do-Quang *et al.*,[32] Parsa and Voth,[33] Lin *et al.*[34] among the most recent ones), but almost all analyses focus on very long fibers with length spanning over many dissipative length scales (hence, finite-size effects must be accounted for). When small fibers are considered,[29] the flow is represented by a model (e.g., random flow) that does not replicate all features of anisotropic turbulence: In a random flow, in particular, vorticity and strain rate are not directly related and this leads to a much weaker preferential alignment. To the best of our knowledge, a clearcut characterisation of length effects for the case of small fibers in wall-bounded turbulence has not been provided yet.

The paper is organised as follows. In Section II, the physical problem considered and the governing equations for fluid and fibers are presented. A short summary of the simulations performed is provided in Section III, followed by the discussion of the statistical observables in Section IV. In this section, in particular, the correlation between the rotational and translational motions of the fibers relative to the surrounding fluid is examined. Finally, conclusions are drawn in Section V.

II. MATHEMATICAL MODELLING AND GOVERNING EQUATIONS

We simulate the motion of rigid fibers in turbulent channel flow using an Eulerian-Lagrangian approach. To make the paper self-contained, in this section, we briefly outline the physical problem under investigation and the governing equations. More details can be found in the work of Zhao *et al.*[25]

The carrier fluid is Newtonian (with dynamic viscosity μ and kinematic viscosity ν) and incompressible (with density ρ). The fluid motion is governed by the following dimensionless mass and momentum conservation equations:

$$\nabla \cdot \mathbf{u} = 0, \qquad \frac{\partial \mathbf{u}}{\partial t} + (\mathbf{u} \cdot \nabla)\mathbf{u} = -\nabla p + \frac{1}{Re_\tau}\nabla^2 \mathbf{u}, \tag{1}$$

where $\mathbf{u}$ and p denote the fluid velocity vector and the pressure, respectively. The frictional Reynolds number is $Re_\tau = hu_\tau/\nu$, with h the channel half-height, the wall-friction velocity $u_\tau = \sqrt{\tau_{wall}/\rho}$ is based on the wall shear stress τ_{wall}. The flow is driven by a constant mean pressure gradient and is unaffected by the presence of the fibers. The present study is therefore one-way coupled and applies only to dilute fiber suspensions.

Fibers are modelled as pointwise rigid prolate spheroids with aspect ratio $\lambda = b/a$, where b and a are the semi-major and semi-minor axes of the spheroid, respectively. Translation and rotation of a single fiber of density ρ_p and mass $m_p = 4\pi a^3 \lambda \rho_p/3$ are governed by the following equations, in vector form:

$$m_p \frac{\mathrm{d}\mathbf{u}_p}{\mathrm{d}t} = \mathbf{F}_D, \tag{2}$$

$$\frac{\mathrm{d}(\mathbf{I} \cdot \boldsymbol{\omega}')}{\mathrm{d}t} + \boldsymbol{\omega}' \times (\mathbf{I} \cdot \boldsymbol{\omega}') = \mathbf{N}'. \tag{3}$$

In Eq. (2), $\mathbf{u}_p = \mathrm{d}\mathbf{x}_p/\mathrm{d}t$ is the translational fiber velocity and $\mathbf{F}_D$ is the drag force acting on the fiber, both formulated in the *inertial* frame of reference $\mathbf{x} = \langle x, y, z \rangle$, with x, y, and z the streamwise, spanwise, and wall-normal flow directions, respectively. In Eq. (3), $\mathbf{I}$ is the moment of inertia tensor, $\boldsymbol{\omega}'$ is the angular velocity of the fiber, and $\mathbf{N}'$ is the torque. Both $\boldsymbol{\omega}'$ and $\mathbf{N}'$ are formulated in the *fiber* frame of reference $\mathbf{x}' = \langle x', y', z' \rangle$ with origin at the fiber center of mass and coordinate axes x', y', and z' aligned with the principal directions of inertia. In the limit of pointwise fibers, the

surrounding flow can be considered as Stokesian and the drag force $\mathbf{F}_D$ can be expressed as

$$\mathbf{F}_D = \mu \mathbf{A}^t \mathbf{K}' \mathbf{A} \cdot (\mathbf{u}_f - \mathbf{u}_p) = \mu \mathbf{A}^t \mathbf{K}' \mathbf{A} \cdot \Delta \mathbf{u}, \tag{4}$$

where $\mathbf{u}_f$ is the fluid velocity at the fiber position, $\mathbf{K}'$ is the resistance tensor in the fiber frame, and $\Delta\mathbf{u}$ is the relative velocity between the fluid and the fiber at the center of mass of the fiber (referred to as slip velocity hereinafter). In Eq. (4), $\mathbf{A}$ denotes the orthogonal transformation matrix which relates the same vector in the two above mentioned frames through the linear transformation $\mathbf{x} = \mathbf{A}\mathbf{x}'$. For a prolate spheroid with z' along the major axis, the off-diagonal elements of $\mathbf{K}'$ are identically zero and the diagonal elements become[35,36]

$$\begin{aligned} k'_{xx} = k'_{yy} &= \frac{16\pi a \sqrt[3]{\lambda^2 - 1}}{(2\lambda^2 - 3)\ln(\lambda + \sqrt{\lambda^2 - 1}) + \lambda\sqrt{\lambda^2 - 1}}, \\ k'_{zz} &= \frac{8\pi a \sqrt[3]{\lambda^2 - 1}}{(2\lambda^2 - 1)\ln(\lambda + \sqrt{\lambda^2 - 1}) - \lambda\sqrt{\lambda^2 - 1}}. \end{aligned} \tag{5}$$

The expression for the hydrodynamic drag force acting on a particle with arbitrary shape was derived by Brenner[37] assuming creeping flow conditions, i.e., low fiber Reynolds number, $Re_p = 2a \mid \Delta\mathbf{u} \mid /\nu$. In agreement with the definition adopted for the fiber response time, the fiber Reynolds number is somewhat arbitrarily based on the semi-minor axis a. Alternative definitions could involve the semi-major axis b or the radius of the volume-equivalent sphere, $r_{p,eq} = a\sqrt[3]{\lambda}$. In our simulations, Re_p is always significantly smaller than unity with the exception of the $St = 100$ particles, for which maximum values slightly above 1 are obtained well inside the buffer region. In this case, underestimation of the drag force would amount to roughly 15% of the Stokes drag for the spherical particles, according to the correction of Schiller and Naumann.[38] Note, however, that equivalent corrections for non-spherical particles are currently unavailable (see also discussion in the work of Zhao *et al.*[25]). To focus on effects of fiber shape and inertia on rotation, gravity was ignored since it would influence the relative motion between fibers and fluid by decorrelating $\mathbf{u}_p$ from $\mathbf{u}_f$. The shear-induced lift force was also ignored, even if it might have a quantitative impact on the statistics since $\mathbf{F}_L/\mathbf{F}_D \simeq O\left(a\sqrt{\frac{1}{\nu}\frac{\partial u}{\partial z}}\right) \simeq O(0.1)$. This choice was motivated by the lack of reliability of the lift force models currently available for ellipsoidal particles:[39] in fact, these models are straightforward extensions of the Saffman model and, for the simulation parameters adopted in the present study, would produce unphysical fiber transfer fluxes away from the wall.[40]

The torque components N'_i can be expressed as follows:

$$\begin{aligned} N'_x &= C_x[(1-\lambda^2)S'_{yz} + (1+\lambda^2)(\Omega'_x - \omega'_x)],\ C_x = \frac{16\pi\mu a^3\lambda}{3(\beta_0 + \lambda^2\gamma_0)}, \\ N'_y &= C_y[(\lambda^2-1)S'_{xz} + (1+\lambda^2)(\Omega'_y - \omega'_y)],\ C_y = \frac{16\pi\mu a^3\lambda}{3(\alpha_0 + \lambda^2\gamma_0)}, \\ N'_z &= C_z(\Omega'_z - \omega'_z),\ C_z = \frac{32\pi\mu a^3\lambda}{3(\alpha_0 + \beta_0)}, \end{aligned} \tag{6}$$

where the parameters α_0, β_0, and γ_0 depend on the aspect ratio λ, and their expressions were first derived by Jeffery[41] for an ellipsoidal particle in creeping motion. In Eq. (6), S'_{ij} and Ω'_i denote elements of the fluid rate-of-strain tensor and rate-of-rotation vector, respectively. The slip spin is defined here as $\Delta\omega'_i = \Omega'_i - \omega'_i$.

The Lagrangian approach just described is essentially an extension to fiber-like particles of the pointwise approach routinely used for dilute suspensions of spherical particles. Due to its simplicity and relatively low computational cost (compared to finite-size particle computations, for instance), this approach is still widely used to simulate two-phase flows in which the collective behaviour of large ensembles of small non-spherical particles ($O(10^6)$) must be taken into account. However, it also has several important limitations, especially in terms of accuracy and reliability of the available force models: The reader is referred to the paper by Zhao *et al.*[25] for a more detailed discussion of such limitations.

In our model, the shape of the fiber is fully characterised by the aspect ratio λ, whereas its ability to interact with the local flow field is parameterised by the Stokes number (the dimensionless particle response time), $St = \tau_p/\tau_f$, where

$$\tau_p = \frac{2}{9}\frac{\rho_p a^2}{\mu} f(\lambda), \quad \text{with} \quad f(\lambda) = \frac{\lambda \ln(\lambda + \sqrt{\lambda^2 - 1})}{\sqrt{\lambda^2 - 1}} \tag{7}$$

is the characteristic time scale of the fiber translational motion[42] and $\tau_f = \nu/u_\tau^2$ is the characteristic time scale of near-wall turbulence. Note that Eq. (7) is valid in the approximation of isotropic fiber orientation, and that $\lim_{\lambda\to 1} f(\lambda) = 1$. Since we are interested in the rotational dynamics of the fibers with respect to the surrounding fluid, it is useful to parameterise also their rotational inertia via a suitable Stokes number, referred to as St_r hereinafter. For spherical particles, it is well known that[43,44]

$$St_r = \frac{3}{10} St. \tag{8}$$

The corresponding relation for fibers, however, is less straightforward since it cannot be based on the assumption of isotropic rotation, which would yield Eq. (8) regardless of the value of λ. Here, we chose to retain the anisotropy of fiber rotational motion in the definition of St_r and to use two different expressions: one for St_r along the minor axis of the fiber frame (referred to as $St_{r,\perp}$ in the following) to quantify the inertial response of the fiber to "tumbling"-like rotation and one along the major symmetry axis of the fiber frame (referred to as $St_{r,\parallel}$) to quantify the inertial response of the fiber to "drilling"-like rotation. Both $St_{r,\perp}$ and $St_{r,\parallel}$ are derived as inverse of the λ-dependent quantities that multiply the slip spin components $\Omega_i' - \omega_i'$ in Eq. (6), therefore assuming constant angular acceleration along each principal axis, the rotational Stokes numbers read as

$$St_{r,\perp} = \frac{3(\beta_0 + \lambda^2\gamma_0)}{16\pi\mu a^3 \lambda(1+\lambda^2)} \frac{I_{x'x'}}{\tau_f} = \frac{9}{40}\frac{\alpha_0 + \lambda^2\gamma_0}{f(\lambda)} St, \tag{9}$$

$$St_{r,\parallel} = \frac{3(\alpha_0 + \beta_0)}{32\pi\mu a^3 \lambda} \frac{I_{z'z'}}{\tau_f} = \frac{9}{20}\frac{\alpha_0}{f(\lambda)} St, \tag{10}$$

with $I_{x'x'} = I_{y'y'} = \frac{(1+\lambda^2)a^2}{5} m_p$ and $I_{z'z'} = \frac{2a^2}{5} m_p$. Additional rotational Stokes numbers could be defined to account for rotation induced by the fluid rate of strain in x' and y', also appearing in Eq. (6). These, however, would be simply equal to $\pm\frac{1+\lambda^2}{1-\lambda^2} St_{r,\perp}$, respectively, and $\frac{1+\lambda^2}{1-\lambda^2} \approx -1$ for the fiber sets considered in the present study.

III. SUMMARY OF SIMULATIONS

Direct numerical simulations of turbulent plane Poiseuille flow are performed at two different Reynolds numbers ($Re_\tau = 150$ and 180) using two independent flow solvers: The UUD-solver, described in detail by Soldati *et al.*[45] and by Soldati and Marchioli,[46] and the NTNU-solver, described by Mortensen *et al.*[43] Both flow solvers use a pseudo-spectral method in the two homogeneous directions. In the wall-normal direction, the UUD-solver uses a Chebyshev-collocation method, whereas the NTNU-solver uses a second-order finite-difference discretisation. The time integration is achieved by means of an explicit second-order Adams-Bashforth scheme. The reference geometry consists of two infinite flat parallel walls separated by a distance $2h$. Periodic boundary conditions are used in the x- and y-directions and no-slip conditions are imposed at the walls. The size of the computational domain, the number of grid nodes, and the grid spacings are provided in Table I.

We tracked swarms of 200 000 fibers with aspect ratio ranging from 3 to 50 and Stokes number ranging from 1 to 100. For comparison purposes, spherical particles characterised by $\lambda = 1$ are also tracked, for a total of 16 cases for each value of Re_τ. All fibers have the same radius on the minor axes $a^+ = 0.36$. These are summarised in Table II, together with an overview of the different parameter combinations in the (Re_τ, St, λ) space that were considered in earlier studies of particle orientation statistics in turbulent channel flow. The corresponding values of the rotational Stokes

TABLE I. Domain size and discretisation for the different Reynolds numbers considered in this study. The entries for the wall-normal grid spacing Δz^+ refer to the smallest mesh size next to the solid walls and the largest grid spacing in the center of the channel.

Re	Domain size	Grid points	Δx^+	Δy^+	Δz^+	Code
150	$4\pi h \times 2\pi h \times 2h$	$128 \times 128 \times 129$	14.72	7.36	0.045-3.68	UUD[45,46]
180	$12h \times 6h \times 2h$	$192 \times 192 \times 192$	11.25	5.63	0.44-2.86	NTNU[43]

TABLE II. Summary of the simulations and overview of earlier studies performed in the same parameter space. Symbols: ■ Present study, ◇ Zhang *et al.*[36] $Re_\tau = 125$, ○ Mortensen *et al.*[44] $Re_\tau = 180$, ⊗ Mortensen *et al.*[43] $Re_\tau = 180$, □ Marchioli *et al.*[47] $Re_\tau = 150$, ▽ Zhao and van Wachem[48] $Re_\tau = 150$, △ Zhao *et al.*[49] $Re_\tau = 180$.

	St					
λ	0.5	1	5	10	30	100
1		□ ■	⊗ □ ■		⊗ □ ■	□ ■
3		□ ■	⊗ ▽ □ ■		⊗ □ ■	□ ■
5			◇			
10	○	□ ■	⊗ □ ■	○	⊗ □ ■	□ ■
30	○			○		
50	○	□ ■	□ ■	○	□ ■	□ ■
≥100		△		△		

numbers are shown in Table III. As one would expect, an increase of fiber length corresponds to an increase (decrease) of $St_{r,\perp}$ ($St_{r,\parallel}$), the two Stokes numbers being equal for spherical particles: Longer fibers are more keen to rotate around their major symmetry axis than to rotate around their minor axes.

The fiber tracking in the UUD solver is based on a fourth-order Runge-Kutta scheme, while the fluid velocities and velocity gradients at fiber position, required to compute the rate of strain and the rate of rotation in Eq. (6), are obtained using sixth-order Lagrangian polynomials. The NTNU solver integrates the fiber equations of motion in time via a second-order Adams-Bashforth scheme, while the local fluid velocities and velocity gradients are interpolated with second-order accuracy. The fiber-wall collision is fully elastic so that a fiber keeps its linear momentum in the two homogeneous directions as well as its angular momentum upon touching the wall. A collision

TABLE III. Values of the rotational Stokes numbers with respect to the fiber's symmetry axis, $St_{r,z'} = St_{r,\parallel}$, and with respect to the minor axis of the fiber, $St_{r,x'} = St_{r,y'} = St_{r,\perp}$.

	St				
λ	1	5	30	100	
1	0.3	1.5	9.0	30.0	$St_{r,\parallel}$
	0.3	1.5	9.0	30.0	$St_{r,\perp}$
3	0.21	1.07	6.44	21.45	$St_{r,\parallel}$
	0.34	1.71	10.28	34.27	$St_{r,\perp}$
10	0.15	0.73	4.40	14.66	$St_{r,\parallel}$
	0.38	1.88	11.30	37.67	$St_{r,\perp}$
50	0.10	0.49	2.93	9.76	$St_{r,\parallel}$
	0.40	2.01	12.04	40.12	$St_{r,\perp}$

occurs every time the distance from the center of mass of a fiber, G, to the closest wall becomes less than the semi-minor axis, a. The same approach was adopted by Marchioli *et al.*[47] and by Zhang *et al.*[36]

All results shown in the following refer to the case $Re_\tau = 150$ (see Table I) unless otherwise stated. The statistics were collected over a time window $\Delta t^+ = 5100$ starting at time $t^+ = 3000$ after fiber injection, and compared one-to-one with those collected at $Re_\tau = 180$ over a time window $\Delta t^+ = 3600$ starting at time $t^+ = 7200$ after fiber injection: no significant quantitative differences were observed. Indeed, within such time windows, fiber rotation has reached the steady state. This is demonstrated by the time evolution of the fiber angular velocity squared, $\overline{(\omega^+)^2}^{bin}$, shown in Fig. 1 for the $St = 100$ fibers (in our simulations, these fibers take longer than all others to achieve a statistically steady rotational motion). The evolution of $\overline{(\omega^+)^2}^{bin}$ is evaluated in three different regions of the channel: the viscous layer ($0 \le z^+ \le 7$), where the mean shear is highest; the buffer layer ($7 < z^+ \le 30$), where Reynolds stresses reach a maximum; and a fluid layer across the channel centerline ($140 \le z^+ \le 160$), where flow conditions are closer to homogeneous and isotropic. It can be observed that, regardless of the flow region, $\overline{(\omega^+)^2}^{bin}$ fluctuates around its steady state value. This value is higher close to the wall, where it is also significantly influenced by the aspect ratio of the fiber: longer fibers rotate at a slower pace. This is a first indication that fiber anisotropy adds to flow anisotropy leading to non-trivial rotational dynamics. Only a modest effect of fiber length is observed in the region across the channel centerline, where the $\overline{(\omega^+)^2}^{bin}$ profiles exhibit a reversed dependence on λ. This is consistent with the recent study by Byron *et al.*[29] who reported a slightly larger rotation of high aspect ratio particles in isotropic turbulence.

IV. RESULTS

Earlier studies of fiber-laden channel flows have shown that inertia plays an important role in determining the translational motion of the fibers as well as their preferential concentration. However, the fiber length was found to produce only quantitative differences in the velocity and concentration statistics.[25,43,47] When the focus is on the rotational motion of the fibers, as in the present study, both inertia and shape become important. The visualisations in Fig. 2 give an impression of the instantaneous fiber rotation in the near-wall region of the turbulent channel flow. Both spherical particles and fibers (with aspect ratio 3) are shown, rendered as circles drawn at the position of the center of mass and coloured based on their spanwise angular velocity, ω_y^+. The background colour

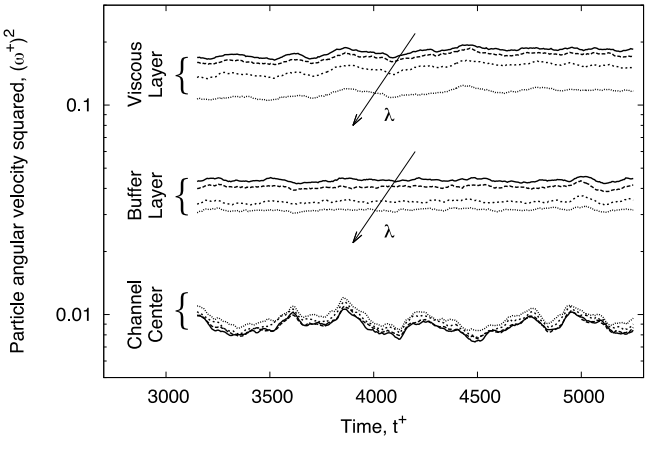

FIG. 1. Time evolution of the conditional fiber angular velocity squared, $\overline{(\omega^+)^2}^{bin}$. Each curve refers to a given value of the aspect ratio for the reference case of $St = 100$ fibers and was computed upon ensemble averaging $(\omega^+)^2$ within three different flow regions: a viscous layer comprised in the fluid bin $0 \le z^+ \le 7$, a buffer layer comprised in the fluid bin $7 < z^+ \le 30$, and a layer across the channel centerline comprised in the fluid bin $140 \le z^+ \le 160$. ———: $\lambda = 1$, – – –: $\lambda = 3$, - - - - -: $\lambda = 10$, · · · · · · · · ·: $\lambda = 50$.

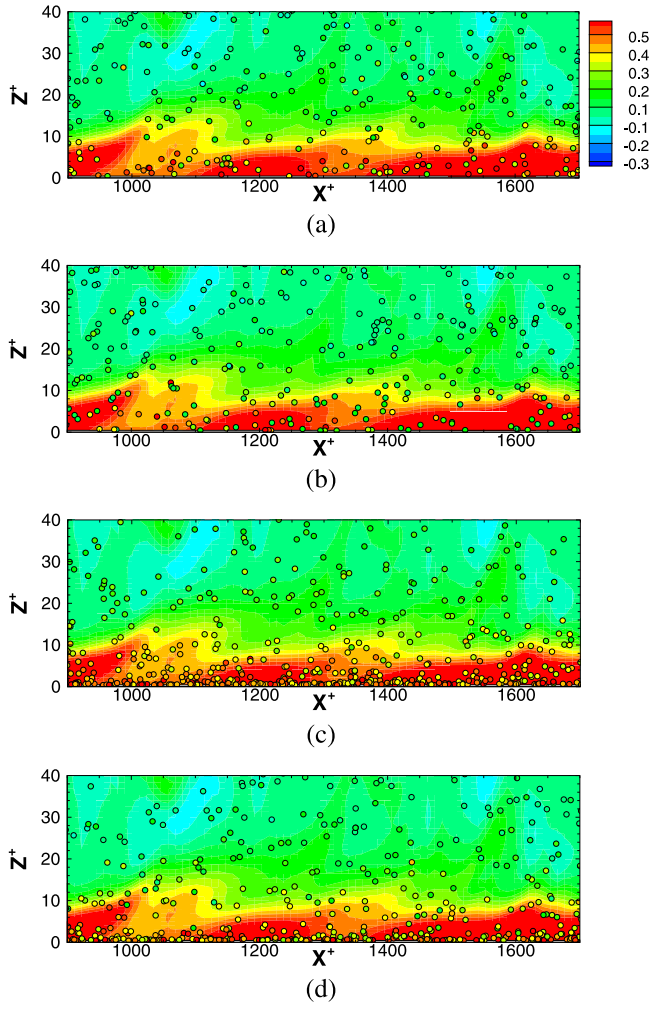

FIG. 2. Snapshot of fiber distribution in the near-wall region of the channel (up to a distance of 40 wall units from the wall), superposed to the instantaneous fluid vorticity field (represented by the spanwise component of the fluid angular velocity Ω_y^+). Fibers are represented by their center of mass and coloured depending on their spanwise angular velocity ω_y^+. (a) and (c) spherical particles with Stokes number $St = 1$ and $St = 100$, respectively; (b) and (d) $\lambda = 3$ fibers with $St = 1$ and $St = 100$, respectively.

contours (which are the same in all four panels since the flow is unaffected by the presence of the fibers) represent the spanwise angular velocity of the fluid, Ω_y^+, much higher in the vicinity of the wall than in the logarithmic region beyond $z^+ \simeq 30$. Any colour difference between a fiber and the surrounding fluid signifies a relative rotation rate, i.e., slip spin. Otherwise, the fiber rotates at exactly the same rate as the fluid.

Inertia has a modest effect on particle motions for $St = 1$, as shown in Figs. 2(a) and 2(b). Most of the spherical particles in Fig. 2(a) seem to rotate at almost the same rate as the surrounding fluid, even in the near-wall region. In Fig. 2(b), a larger fraction of the fibers exhibits a different colour than the background suggesting that, already at $\lambda = 3$, fibers are unable to adapt to near-wall fluid rotation. Longer fibers ($\lambda \geq 10$ in our simulations, results not shown) exhibit the same tendency.

The more inertial particles ($St = 100$, Figs. 2(c) and 2(d)) also follow the fluid rotation partially. Regardless of their shape, these particles are known to accumulate in low-speed near-wall streaks as long as the pointwise assumption holds, see, e.g., the works of Marchioli and Soldati[50] and Marchioli *et al.*[47] As a result, particle concentration is clearly higher in the viscous wall layer than elsewhere in the channel. Within this layer, preferential distribution in low-speed streaks makes almost all particles and fibers rotate slower than the ambient fluid. However, in the buffer layer

($7 \leq z^+ \leq 30$), a significant fraction of the particles are seen to rotate faster than the fluid and the slip spin $\Delta\omega_y^+ = \Omega_y^+ - \omega_y^+$ becomes negative. A physical explanation of this unexpected behaviour will be given in Section IV B.

The inability of the fibers to passively follow the fluid rotation at low Stokes numbers is probably associated with their orientation in the flow field. A thorough understanding of fiber rotation relative to the surrounding fluid thus requires a preliminary analysis of fiber orientation, in view of its role in determining the drag force and the torque acting on the fibers. Moreover, in practical applications such as papermaking, the resulting orientations of the cellulose fibers determine the quality of the final product.[2]

A. Fiber orientation

To explore fiber orientation (namely, fiber alignment with the flow), we adopt the orientation angles used by Zhang *et al.*,[36] Mortensen *et al.*,[43,44] and Marchioli *et al.*[47] The orientation angle θ_i is defined as the angle between the major axis of the prolate spheroid (z' in the particle frame) and the axes of the co-moving frame of reference, indicated as x'', y'', and z'' in Fig. 3(a). The co-moving frame origin is at the mass center of the fiber[36,43] and the coordinate axes are parallel to those of the inertial frame. Fiber orientation can be measured by $\langle |\cos(\theta_i)| \rangle$, referred to as direction cosine hereinafter.

The polar diagrams in Figs. 3(b)-3(d) show the probability density functions (PDFs) of the orientation angles for the $St = 1$ fibers and give a first impression of the aspect ratio effect on preferential orientation. To highlight the effect of the flow anisotropy, only a thin slice of the buffer region just outside the viscous layer is considered ($7 \leq z^+ \leq 10$). The mean values of the orientation angles measured in this slice are shown, for all fiber sets, in Table IV. Examination of Fig. 3 and Table IV suggests that, in our problem, short fibers undergo a more complex rotation than long

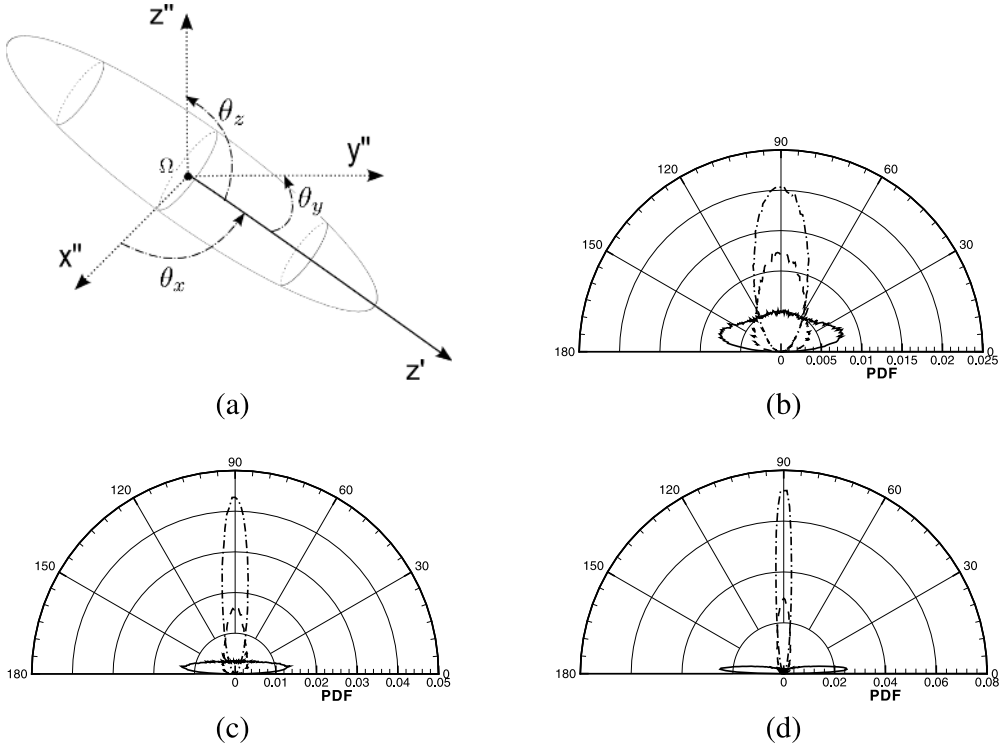

FIG. 3. Polar diagrams showing fiber orientation in the near-wall region $7 \leq z^+ \leq 10$. Fiber orientation is given here by the PDF of the angle θ_i between the coordinate axis x_i'' of the co-moving reference frame and the symmetry axis z' of the fiber, as shown in panel (a). Only fibers with $St = 1$ are considered. (b) $\lambda = 3$; (c) $\lambda = 10$; (d) $\lambda = 50$. ———: θ_x, – – –: θ_y, – · – · –: θ_z.

TABLE IV. Mean value of the fiber orientation angles, θ_i, computed as average of the absolute value of the corresponding directions cosines.

	St			
λ	1	5	30	100
	Orientation angle, θ_x			
3	43.21	39.07	45.48	45.88
10	33.81	32.75	44.36	45.25
50	22.49	24.36	43.37	45.09
	Orientation angle, θ_y			
3	59.17	76.58	81.92	82.42
10	61.80	69.07	75.62	74.56
50	70.90	71.74	66.95	68.24
	Orientation angle, θ_z			
3	70.92	58.66	48.24	47.56
10	79.37	72.90	53.93	53.65
50	82.98	79.87	61.98	59.08

fibers. For the shortest fibers ($\lambda = 3$, Fig. 3(b)), the PDF peaks at $\theta_x \simeq 15°$ but the mean value of θ_x is about 43°. Several short fibers may even align with the spanwise direction, in agreement with the laboratory measurements,[31] which were taken in the same range of values for both the fluid and particle simulation parameters. The tendency to attain a preferential orientation in the mean-flow direction increases with the aspect ratio: The longest fibers ($\lambda = 50$, Fig. 3(d)) lie almost entirely in a wall-parallel plane ($\theta_z \simeq 90°$) and tend to align with the streamwise direction ($\theta_x \simeq 0°$ or 180°). This result is again in agreement with the experimental findings of Abbasi-Hoseini *et al.*[31]

The translational and rotational motions of the fibers will intuitively depend on how they orient within the flow. In particular, fiber alignment with the mean flow direction can be measured by the direction cosine $|\cos(\theta_x)|$, which is the component of the fiber orientation unit vector **p** in the streamwise x-direction. Previous investigations[36,43,47] have demonstrated that prolate spheroids with inertia orient preferentially with the mean flow direction in the near-wall region, this tendency being stronger for high aspect ratios. More recently, Zhao *et al.*[49] have shown that fiber preferential orientation becomes independent of fiber length for aspect ratios above 100. The $\langle|\cos(\theta_x)|\rangle$ profiles shown in Fig. 4(a), which refer to the $St = 1$ fibers, indicate that such trends are even more pronounced at modest inertia. The dependence of the fiber-to-flow alignment on *St* at fixed aspect ratio ($\lambda = 10$ is chosen here) is shown in Fig. 4(b). While it is confirmed that an increase of inertia reduces preferential orientation in the streamwise direction, a "saturation" of inertial effects seems to occur for Stokes numbers above 100. Note that fibers always orient randomly in the core region of the channel, with $\langle|\cos(\theta_x)|\rangle \simeq 0.5$ irrespective of aspect ratio or inertia.

The insets in Fig. 4, which show the wall-normal behaviour of $\langle|\cos(\theta_z)|\rangle$ (component of **p** in the wall-normal direction), indicate that the near-wall gradual increase (decrease) of $\langle|\cos(\theta_x)|\rangle$ is accompanied by a reduction (an increase) of $\langle|\cos(\theta_z)|\rangle$. This implies that fibers with either high aspect ratio or low inertia are almost entirely confined in wall-parallel (x, y)-planes in regions of strong mean shear.

B. Statistical moments of the slip spin

In this section, we characterise from a statistical point of view the slip spin, and we try to link the statistical moments of this quantity with the observations on fiber orientation made in Sec. IV A. The wall-normal behaviour of the mean slip spin, $\langle\Delta\omega_y\rangle^+$, is shown in Fig. 5. Here, brackets denote quantities averaged over the homogeneous directions and in time. Only the spanwise component is

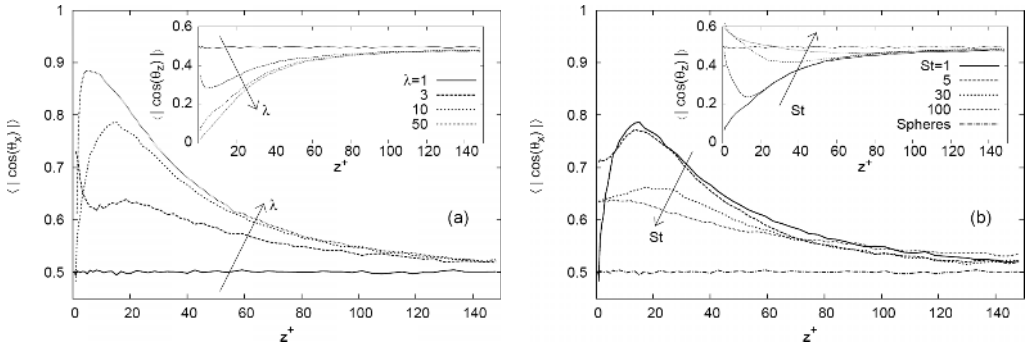

FIG. 4. Wall-normal behaviour of the streamwise direction cosine $\langle|\cos(\theta_x)|\rangle$. The insets show the behaviour of the wall-normal direction cosine $\langle|\cos(\theta_z)|\rangle$. (a) Effect of fiber length λ for $St = 1$; (b) effect of fiber inertia for $\lambda = 10$.

discussed since the streamwise and the wall-normal ones are zero across the channel cross section. All fiber sets are considered. There is a clear effect of fiber length on $\langle\Delta\omega_y\rangle^+$ close to the wall, notably inside the buffer layer, where fiber alignment along the mean flow direction is strongest. In this region, the relative rotation between fibers and surrounding fluid increases monotonically with λ for all St. We remark that such a strong length-dependent effect is not observed for the translational slip velocity.[25] Outside the buffer layer ($z^+ > 50$ in our simulations), $\langle\Delta\omega_y\rangle^+$ vanishes regardless of St and λ indicating that fibers and fluid have (on average) the same rate of rotation, the latter being unaffected by anisotropy no matter if due to the flow or due to the particles. The

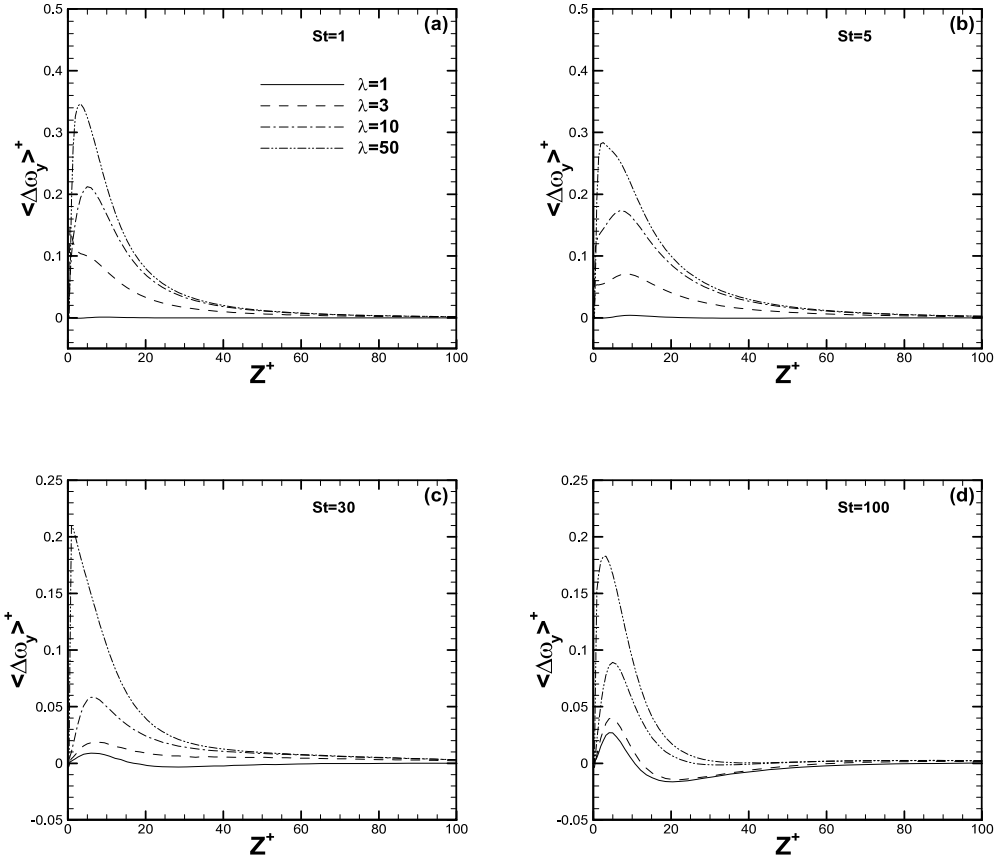

FIG. 5. Effect of fiber inertia and length on the mean spanwise slip spin, $\langle\Delta\omega_y\rangle^+$. (a) $St = 1$; (b) $St = 5$; (c) $St = 30$; (d) $St = 100$. ———: $\lambda = 1$, – – –: $\lambda = 3$, – · – · –: $\lambda = 10$, – · · – · · –: $\lambda = 50$.

near-wall increase of $\langle \Delta\omega_y \rangle^+$ with λ is due to the fact that, for a given value of St, the angular velocity of fibers, $\langle \omega_y \rangle^+$ (not shown), decreases as λ increases, whereas the fluid angular velocity seen by the fibers, $\langle \Omega_{y@p} \rangle^+$ (not shown), remains the same regardless of fiber rotational inertia. The tendency of fibers with high rotational inertia to spin slower than the surrounding fluid resembles that observed for the slip velocity, which is larger for fibers with high translational inertia.[25] Effects on $\langle \omega_y \rangle^+$ due to fiber translational inertia are of course equally significant and lead to a decrease of $\langle \Delta\omega_y \rangle^+$ with increasing St for all aspect ratios. Note that the slip spin is always positive along the wall-normal direction for fibers with small inertia ($St \leq 5$) or large length ($\lambda \geq 10$) but can become negative for fibers with large inertia ($St \geq 30$) and short length ($\lambda \leq 3$). In the latter case, fibers are found to lead fluid rotation and spin faster in the buffer layer (more precisely, in the region $10 < z^+ < 50$). Otherwise, fibers always lag the fluid, as one would intuitively expect. The occurrence of negative slip spin (particularly evident in Fig. 5(d)) is due to a combined effect of high translational inertia and low rotational inertia. This effect is examined in Fig. 6, where we show a scatter plot of the instantaneous values of the spanwise slip spin, $\Delta\omega_y^+$, versus the wall-normal velocity of the fibers, w_p^+. Only the $St = 100$ fibers are considered: short fibers with $\lambda = 3$ in panel (a), also representative of the behaviour of spherical particles; long fibers with $\lambda = 50$ in panel (b). The plot was obtained by counting only the fibers within the fluid slab $10 \leq z^+ \leq 30$, where the largest negative values of $\langle \Delta\omega \rangle^+$ are observed (see Fig. 5(d)). The red area in Fig. 6(a) falls in the fourth quadrant and represents fibers that spin faster than the fluid ($\Delta\omega_y^+ < 0$) while moving away from the wall (${w_p}^+ > 0$). This indicates a clear tendency of short fibers (and spherical particles as well, not shown) to enter the monitor slab with high spanwise spin when coming from the viscous sublayer, which is the region of the flow where spin is the largest due to wall-induced flow anisotropy as shown in Fig. 2. Once they have entered the buffer region, they keep spinning faster than the fluid due to the memory effect associated with their high rotational inertia ($St_{r,\perp} \simeq 34$ for the $\lambda = 3$ fibers). Long fibers, on the contrary, exhibit a much weaker tendency to enter the monitor slab with higher-than-fluid spanwise spin. The scatter plot in Fig. 6(b) is more symmetric with respect to the horizontal $\Delta\omega_y^+ = 0$ axis, across which the red area is located. We remark that this finding is not dependent on the specific fiber-wall collision model adopted in the simulations, in which a collision occurs every time the distance from the center of mass of a fiber to the closest wall becomes less than the semi-minor axis. However, the near-wall statistics might be influenced by a more realistic collision model, for example, if the occurrence of collision also involves the semi-major axis.[51]

The trends observed in Fig. 5, especially that in Fig. 5(a), can be interpreted in terms of the mean rotational slip when a non-inertial fiber rotates in uniform shear in the (x, z)-plane. Assuming that the fiber is initially oriented in the streamwise direction, the resulting Jeffery orbiting gives rise to a mean rotational slip velocity of 0.2017, 0.4009, and 0.4791 about the vorticity axis for fibers

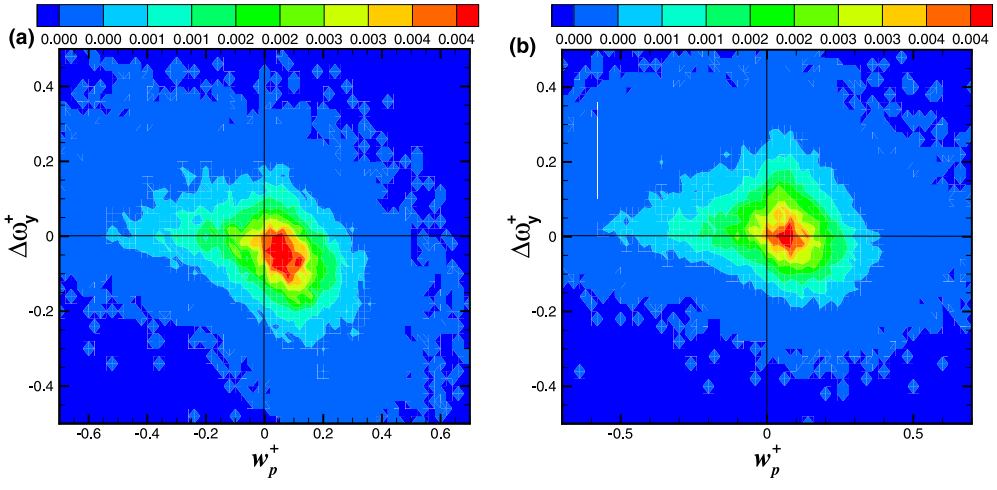

FIG. 6. Scatter plots of the instantaneous spanwise slip spin, $\Delta\omega_y^+$, versus particle wall-normal velocity, w_p^+, conditionally sampled at the $St = 100$ fiber positions. Only fibers in the region $10 \leq z^+ \leq 30$ are considered. (a) $\lambda = 3$; (b) $\lambda = 50$.

with aspect ratios $\lambda = 3$, 10, and 50, respectively (the mean slip is zero for spherical particles). This trend of increasing rotational slip with increasing elongation is consistent with the observations in Fig. 5(a) for the least inertial fibers. Similar findings for non-inertial fiber rotation in turbulent channel flow have been reported by Challabotla *et al.*[6] They claimed that the substantial deviations of mean spin of long fibers relative to the local fluid rotation near the channel walls are attributed to Jeffery-like orbiting and this reflects the importance of mean shear on fiber rotation in wall turbulence. In the present study, we can conclude from Fig. 5 that the slip spin of inertial fibers with a given aspect ratio is also strongly dominated by the mean shear, and moreover, relatively weakly influenced by fiber inertia and interactions with near-wall turbulence structures. Additionally, we would like to point out the importance of the preferential orientation of the fibers, which in combination with the near-wall mean shear results in different fiber rotations. The preferential fiber orientations, as shown in Fig. 4, depend on fiber inertia, shape, and distance from the wall.

To understand how intermittent is fiber rotation relative to the fluid, it is useful to compare the mean slip spin profiles of Fig. 5 with the corresponding root mean square (rms) values. These are shown in Figs. 7–9. We start the analysis from the rms of the spanwise slip spin, $rms(\Delta\omega_y^*)^+$, shown in Fig. 7, where superscript $*$ represents a fluctuation (i.e., $\omega_i^* = \omega_i - \langle\omega_i\rangle$). First of all, we notice that even spherical particles (solid lines) rotate at a different rate with respect to that of the fluid, this tendency being more distinct for high St in accordance with Mortensen *et al.*[55] Such finding may provide useful indications for the development of reliable two-way coupling models in which also torque coupling between the phases, besides momentum coupling, is taken into account.[52] For small values of particle translational inertia (panels (a) and (b) in Fig. 7), short fibers ($\lambda = 3$, dashed lines) are characterised by an abrupt increase of $rms(\Delta\omega_y^*)^+$ with respect to spherical particles. The increase of rms is much smaller for further increase of the aspect ratio, becoming in fact negligible

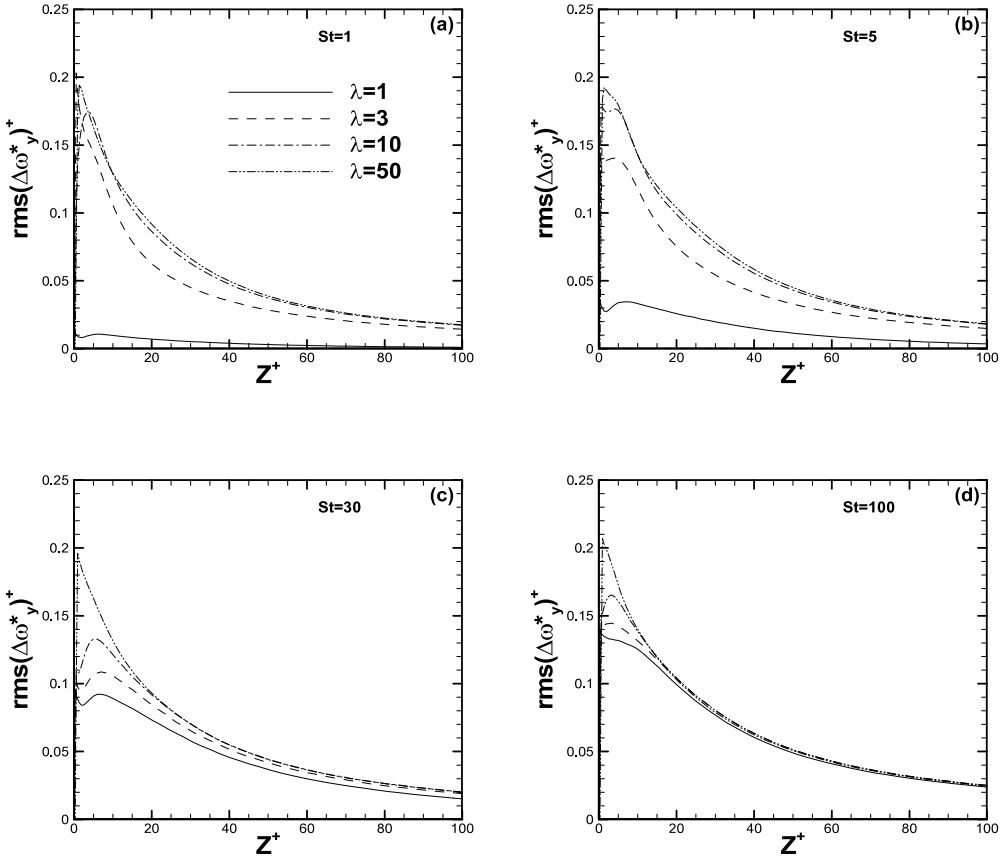

FIG. 7. Effect of fiber inertia and length on spanwise slip spin rms, $rms(\Delta\omega_y^*)^+$. (a) $St = 1$; (b) $St = 5$; (c) $St = 30$; (d) $St = 100$. Lines as in Fig. 5.

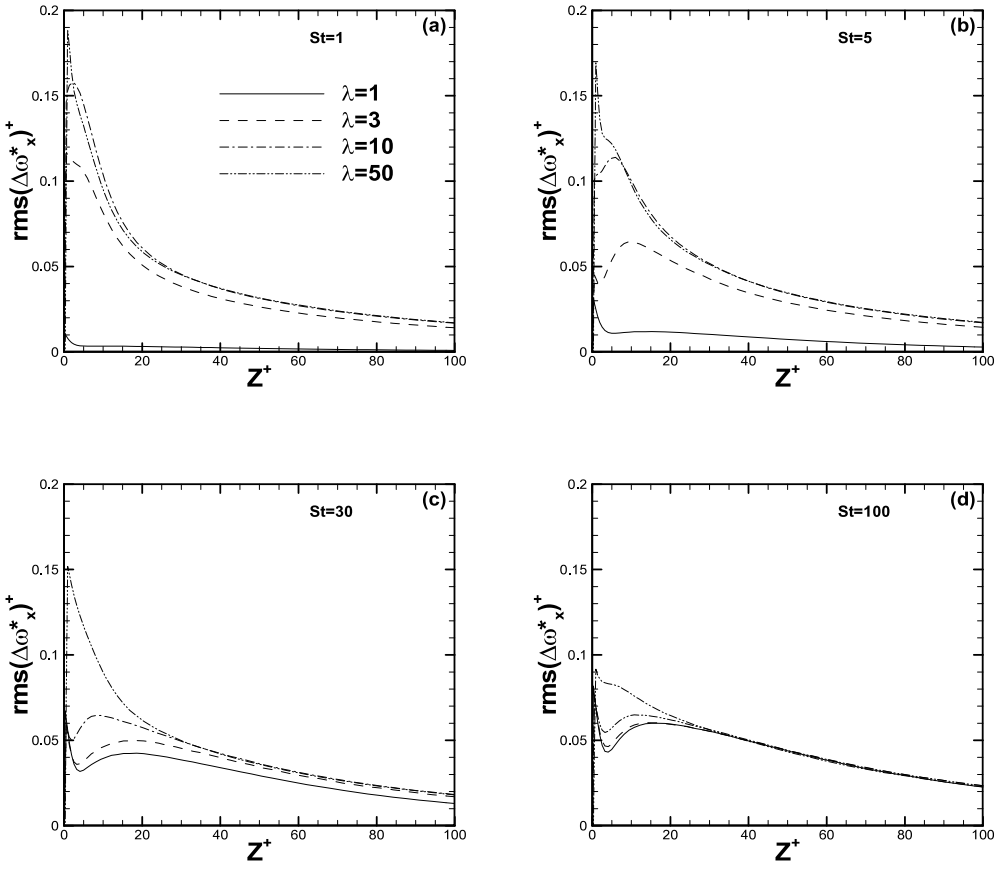

FIG. 8. Effect of fiber inertia and length on streamwise slip spin rms, $rms(\Delta\omega_x^*)^+$. (a) $St = 1$; (b) $St = 5$; (c) $St = 30$; (d) $St = 100$. Lines as in Fig. 5.

from $\lambda = 10$ to $\lambda = 50$. Note that this dampening of λ-effects for fiber with high inertia ($St \geq 30$) was not observed for $\langle\Delta\omega_y\rangle^+$ in Fig. 5. Inertial effects on $rms(\Delta\omega_y^*)^+$ are observed only with short fibers. An increase of St for long fibers $\lambda \geq 10$ does not change much the rms profiles. Indeed, all profiles collapse beyond $z^+ \simeq 20$ for the $St = 100$ fibers. When both inertia and length become large (large St and large λ), we observe that $rms(\Delta\omega_y^*)^+$ is significantly larger than, or at least comparable to, $\langle\Delta\omega_y\rangle^+$: this implies that a given directional component of the instantaneous spanwise slip spin may easily attain the sign opposite to that of the mean value. A similar phenomenon was observed for the slip velocity vector[53] and indicates that reliable closure models aimed at predicting fiber motion in wall-bounded turbulence in two-phase computational fluid dynamics calculations should not be based on mean values of slip velocity and/or slip spin.[54] This conclusion is further corroborated by the results we obtain for the rms of the streamwise slip spin component, $rms(\Delta\omega_x^*)^+$, shown in Fig. 8. The behaviour of the $rms(\Delta\omega_x^*)^+$ profiles is generally similar to that already discussed for $rms(\Delta\omega_y^*)^+$, but now compare with a zero mean value. Fig. 8 shows clearly that a small anisotropy in fiber shape is sufficient to produce strong fluctuations in the rotational motion of the fiber around the streamwise axis (typically drilling), provided that the inertia of the fiber is not too large ($St \leq 5$ in our simulations).

A more complex dependence of rms values on inertia and shape is observed for the wall-normal component, $rms(\Delta\omega_z^*)^+$, shown in Fig. 9. First, in almost all cases, we notice that $rms(\Delta\omega_z^*)^+$ drops to zero close to the wall instead of reaching its maximum value. Considering also that $\langle\Delta\omega_z\rangle^+ = 0$ everywhere across the channel, this implies that there is little or no relative rotation between fibers and fluid around the wall-normal axis close to the wall. Since also the rms of the wall-normal fluid spin drops to zero at the wall (not shown), we conclude that the fibers cannot change their alignment

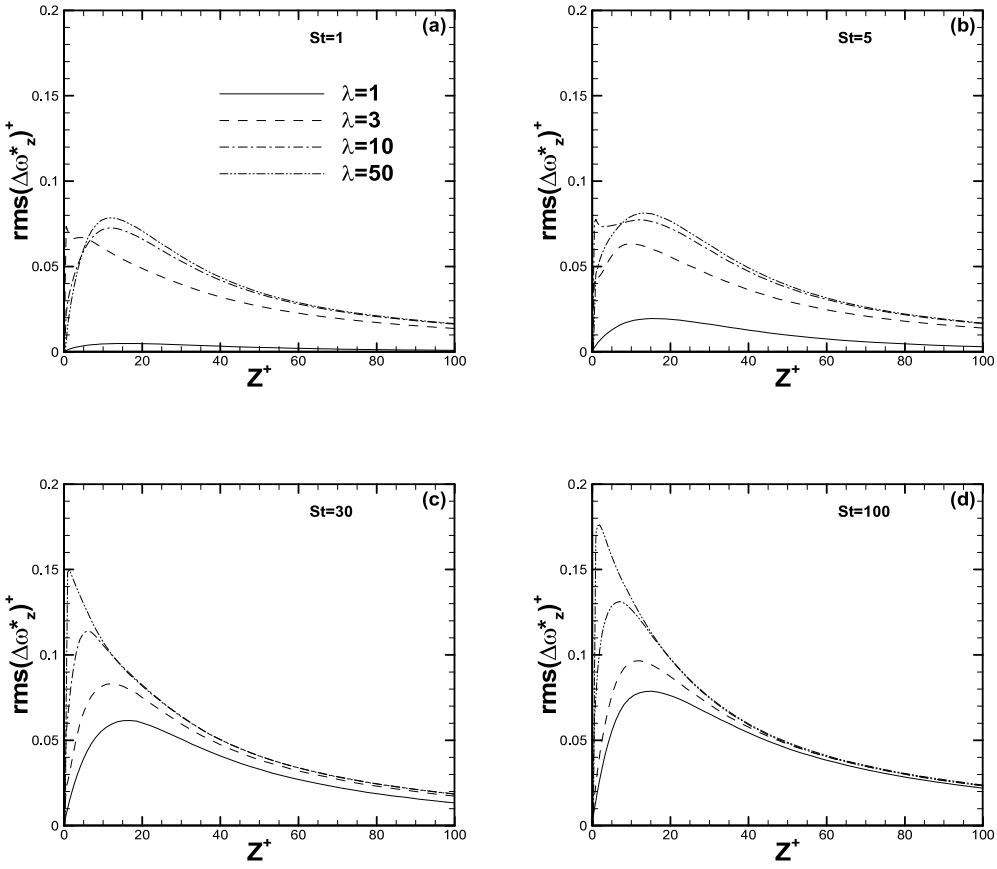

FIG. 9. Effect of fiber inertia and length on wall-normal slip spin rms, $rms(\Delta\omega_z^*)^+$. (a) $St = 1$; (b) $St = 5$; (c) $St = 30$; (d) $St = 100$. Lines as in Fig. 5.

relative to the mean flow direction (by rotating around the z-axis) once they are trapped in the viscous sublayer. Therefore, if any preferential alignment with the mean flow direction occurs, it must be "imposed" to the fibers during their motion to the wall, namely, by the sweep events that bring the fibers towards the wall. In case of small fiber inertia (panels (a) and (b)), there are two exceptions to the general trend just described, observed also in the independent simulation run at $Re_\tau = 180$ with the NTNU code: $St = 1$ fibers with $\lambda = 3$ (dashed line in Fig. 9(a)) and $St = 5$ fibers with $\lambda = 10$ (dotted-dashed line in Fig. 9(b)). Unfortunately, we are currently unable to explain such deviations. In the case of large fiber inertia (panels (c) and (d)), we notice that the location at which the peak of $rms(\Delta\omega_z^*)^+$ occurs shifts towards the wall as λ increases: this is due to the increase of fiber rotational inertia, which prevents the dampening of slip spin fluctuations observed for short fibers in the buffer layer.

C. Spin correlation coefficients

We have so far dealt with how the slip spin depends on fiber inertia and length, namely, on the Stokes number St and on the aspect ratio λ. Another means to study differences between fluid spin Ω_i and fiber spin ω_i is the spin correlation coefficient $\langle\omega_i^*\Omega_i^*\rangle^2/\langle\omega_i^*\rangle^2\langle\Omega_i^*\rangle^2$, where the index i corresponds to either of the three coordinate directions (i.e., no summation is implied here). The correlation coefficient becomes equal to unity in the case of a fiber that passively follows the fluid motion, i.e., the slip spin is zero. The covariance of the fluid and particle spin is related to the slip spin by the relation $\langle\Delta\omega_i^*\rangle^2 = \langle\Omega_i^*\rangle^2 - 2\langle\Omega_i^*\omega_i^*\rangle + \langle\omega_i^*\rangle^2$, suggesting that the slip spin increases when the particle spin becomes more and more decorrelated from the local fluid spin. In Fig. 10,

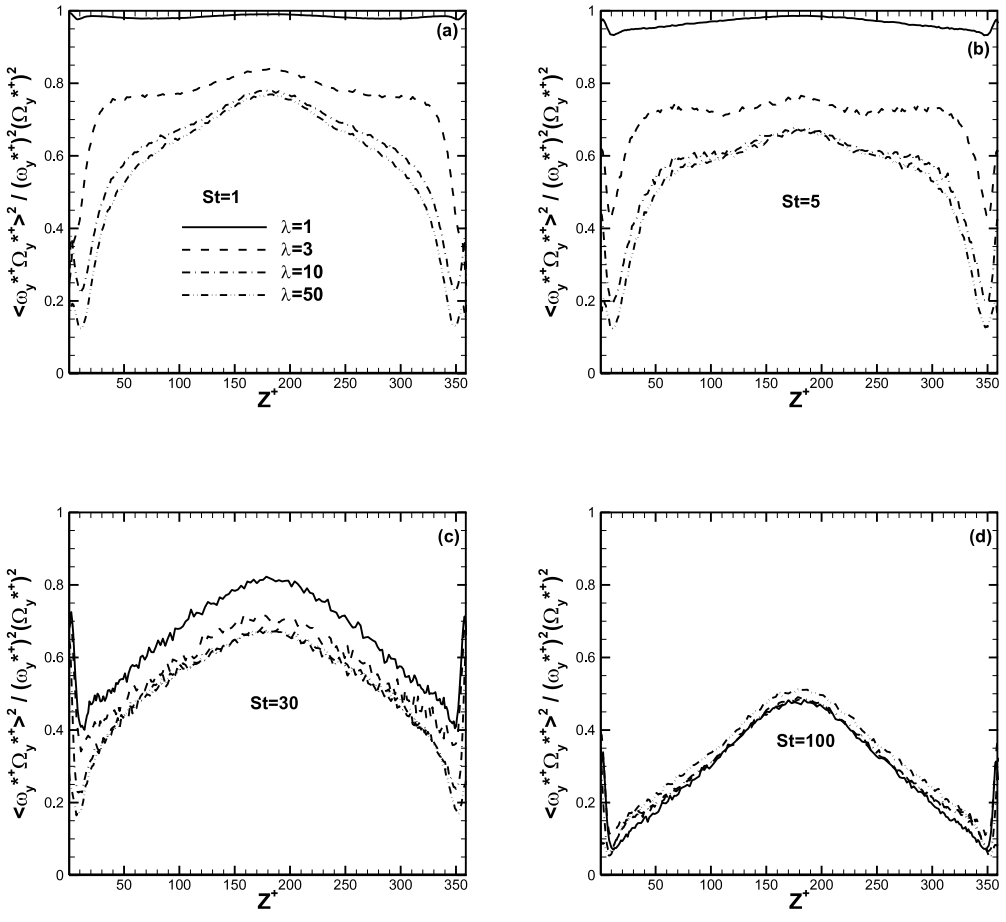

FIG. 10. Effect of fiber inertia and length on the spanwise correlation $\langle\omega_y^{*+}\Omega_y^{*+}\rangle^2/\langle\omega_y^{*+2}\rangle\langle\Omega_y^{*+2}\rangle$. (a) $St = 1$; (b) $St = 5$; (c) $St = 30$; (d) $St = 100$. Lines as in Fig. 5.

we examine the correlation coefficient for all fiber sets, limiting the discussion to the spanwise component, $\langle\omega_y^{*+}\Omega_y^{*+}\rangle^2/\langle\omega_y^{*+2}\rangle\langle\Omega_y^{*+2}\rangle$. In the case of small inertia ($St = 1$, Fig. 10(a)), the correlation coefficient for spherical particles is close to unity all across the channel. This finding is fully consistent with the results shown in Fig. 7(a) and with those reported by Mortensen *et al.*,[55] implying that spheres rotate along with the fluid similar to inertia-free tracers. However, the correlation coefficient is significantly reduced already for $\lambda = 3$ (dashed lines), especially in the near-wall region. The gradual decorrelation continues with increasing aspect ratios, but seems to saturate for $\lambda > 50$. The distinct minimum at $z^+ \simeq 10$ is where the highest decorrelation takes place and this is fairly close to the position of maximum slip spin $\langle\Delta\omega_y\rangle^+$ in Fig. 5(a). This saturation effect is apparently associated with the observation made by Zhao *et al.*[49] that the orientation statistics for long fibers become independent of length as long as λ exceeds 100.

When the aspect ratio is kept constant, the correlation coefficient decreases monotonically with increasing Stokes number. A substantial decorrelation is achieved for the most inertial particles all across the channel in Fig. 10(d). At this particular Stokes number ($St = 100$), the shape effect is almost negligible and the decorrelation is achieved due to inertia alone. Note that the results reported in Fig. 10 are in accordance with the Cauchy-Schwartz inequality $\langle\omega_y^{*+}\Omega_y^{*+}\rangle^2 \le \langle\omega_y^{*+2}\rangle\langle\Omega_y^{*+2}\rangle$ and resemble those obtained for the translational velocity fluctuations of fluid and fibers by Zhao *et al.*[25] In that paper, we pointed out that the condition of particle-fluid covariance being equal to the intensity of particle velocity fluctuations in a given flow direction is not sufficient to ensure that particles passively follow the fluid motion.

D. Correlation between slip spin and slip velocity

The statistics presented in Secs. IV A–IV C show how fiber inertia and fiber length affect fiber rotation relative to fluid rotation. This twofold effect is not observed for the translational slip velocity, which is strongly dependent on inertia[53] but only modestly dependent on aspect ratio.[25] We can thus expect that such different dependencies on the fiber length might play a role in decoupling translational motion from rotational motion. To verify this possibility, we examine how the rotational slip velocity $\Delta\boldsymbol{\omega}$ correlates with the translational slip velocity $\Delta\mathbf{u}$. Such analysis may have practical relevance for the modelling of fiber suspension flows.

One may conjecture that the correlation between the spanwise component of the slip spin $\Delta\omega_y$ and the streamwise component of the translational slip velocity Δu_x may be of major significance. Such scatter plots are shown in Fig. 11 for particles with significant inertia (St = 30) embedded in a near-wall layer between $3 \le z^+ \le 7$, i.e., where viscous shear dominates over turbulent shear stresses and where significant slip velocities and slip spin are observed. A striking effect of particle aspect ratio can immediately be observed by comparing the four different panels. The spherical particles in Fig. 11(a) show a clear tendency to sample regions where $\Delta\omega_y^+$ and Δu_x^+ are both either positive (first quadrant) or negative (third quadrant). This means that an inertial sphere either translates and rotates faster than the ambient fluid or translates and spins slower than its surroundings, giving anyhow rise to a positive correlation or covariance $\Delta\omega_y^+\Delta u_x^+$.

This tendency is gradually reduced with increasing aspect ratios. The teardrop shape of the scatter contours is deformed and becomes more symmetric with respect to the $\Delta\omega_y$-axis, i.e., about

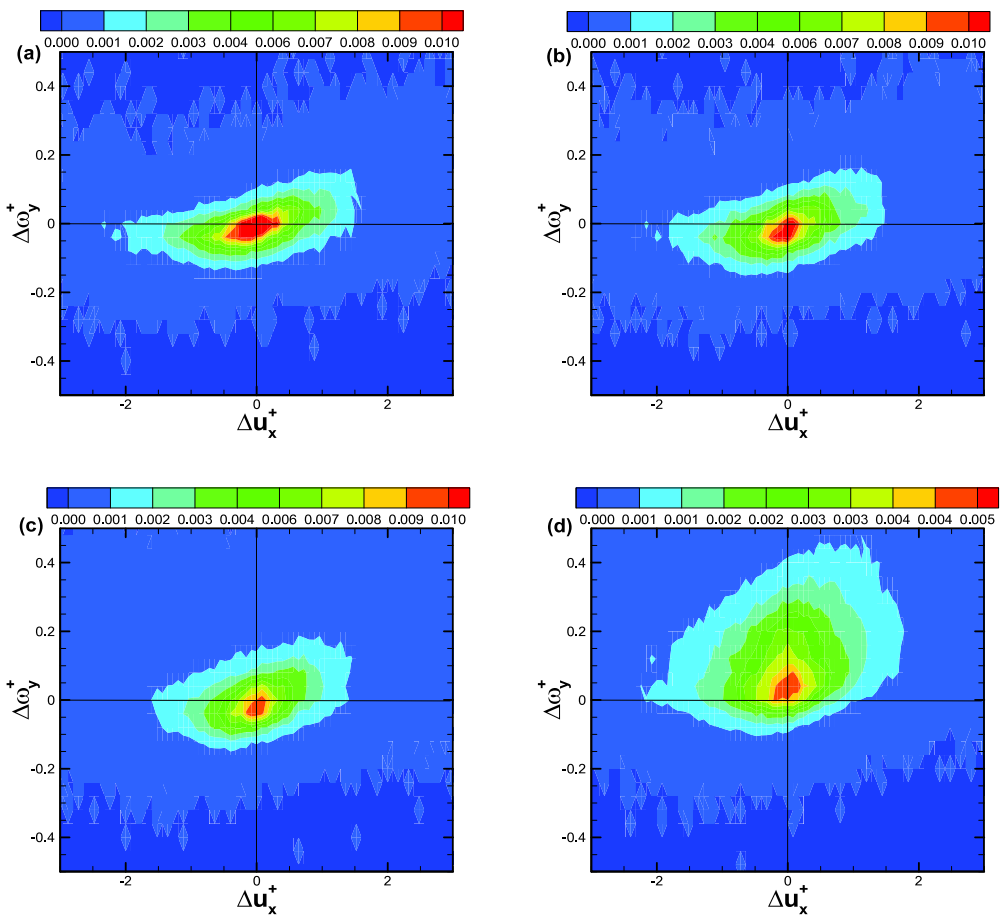

FIG. 11. Effect of fiber elongation on the scatter plots of the instantaneous spanwise slip spin, $\Delta\omega_y^+$, versus streamwise slip velocity, Δu_x^+, conditionally sampled at the $St = 30$ fiber positions. Only fibers in the region $3 \le z^+ \le 7$ are considered. (a) $\lambda = 1$; (b) $\lambda = 3$; (c) $\lambda = 10$; (d) $\lambda = 50$.

$\Delta u_x^+ = 0$. The correlation is thereby weakened and the long fibers are observed to attain positive slip spin regardless of their slip velocity Δu_x^+. The observation that the long fibers rotate slower than the surrounding fluid ($\Delta\omega_y^+ > 0$) suggests that the longest fibers are more reluctant to spanwise rotation. Notice that the boundary conditions used at the channel walls in this study do not impose any geometrical constraints on the fiber rotation and even the longest fibers are allowed to rotate freely even in the immediate vicinity of the walls. These findings are therefore solely due to the dynamical behaviour of the inertial fibers in wall-bounded turbulence.

Let us recall that, on average, fibers in the near-wall region move faster than the local fluid ($\Delta u_x^+ < 0$) mainly because of the high momentum gained in core region of the channel. Negative slip spin $\Delta\omega_y^+$, on the contrary, results from the spin-up in the high-vorticity layer adjacent to the channel walls. Thus, if a fiber is convected to the wall by a sweeping event, both the slip velocity Δu_x^+ and the slip spin $\Delta\omega_y^+$ will be positive. Such events populate the first quadrant of the scatter plots in Fig. 11. On the contrary, a fiber carried along by an ejection will most likely be characterised by $\Delta u_x^+ < 0$ and $\Delta\omega_y^+ < 0$, therefore contributing to the third quadrant of the scatter plots. However, if the fiber is sufficiently long, it can no longer be spun up to match the rapidly rotating fluid, as demonstrated by the monotonic increase of the peak values in Fig. 5(d).

To examine further the fiber-to-fluid rotational dynamics, in Fig. 12, we also scrutinise the correlation between spanwise slip velocity Δu_y^+ and streamwise slip spin $\Delta\omega_x^+$ in the same near-wall region as in Fig. 11. The elongation of the fibers has once again a substantial influence on the scatter plots. For spherical particles in Fig. 12(a), and also for the relatively short fibers in Figs. 12(b) and 12(c), there is a clear tendency to sample regions with positive (negative) values of $\Delta\omega_x^+$ and negative (positive) values of Δu_y^+. This populates the second and fourth quadrants and give rise to a negative covariance $\Delta\omega_x^+\Delta u_y^+$. However, for very long fibers, e.g., the $\lambda = 50$ fibers in Fig. 12(d), the scatter plot becomes symmetric and the covariance between $\Delta\omega_x^+$ and Δu_y^+ vanishes, even if the two quantities are not independent (when one attains large values, the other tends to attain small values).

Based on the findings from Figs. 11 and 12, the gradually reducing correlation between the slip velocity and slip spin in the near-wall region for longer fibers indicates that the force and torque will only be weakly correlated at sufficient large aspect ratios. This suggests that one can model the translational motion of long fibers without any consideration of the rotational motion as long as the focus is on the translational motion and on fiber clustering.

E. Transfer of rotational energy

In Secs. IV B–IV D, we have exploited the slip spin to scrutinise the rotational dynamics of rigid inertial fibers with respect to the surrounding fluid in anisotropic turbulence. This observable, however, can also be related to the overall rotational energy (angular kinetic energy) of the fibers $E_{rot} = \frac{1}{2}\omega_i I_{ij}\omega_j$ and to its rate of change in time, $\dot{E}_{rot}$. This latter quantity is frame invariant and arises as a result of the mechanical (rotational) work done by a torque acting on a fiber. The rate of change of fiber enstrophy ω^2 can be easily obtained from the vector Eq. (3), written in the fiber frame, upon multiplication by $\boldsymbol{\omega}'$. After some simple algebra, it can be shown for an axisymmetric fiber that

$$\frac{1}{2}\frac{\mathrm{d}\omega^2}{\mathrm{d}t} = \frac{1}{2}\frac{\mathrm{d}(\omega')^2}{\mathrm{d}t} = \frac{\omega_x' N_x'}{I_{x'x'}} + \frac{\omega_y' N_y'}{I_{y'y'}} + \frac{\omega_z' N_z'}{I_{z'z'}} =$$

$$\frac{C_x(1+\lambda^2)}{I_{x'x'}}\left[\frac{1-\lambda^2}{1+\lambda^2}(\omega_x' S_{yz}' - \omega_y' S_{xz}') + \omega_x'\Delta\omega_x' + \omega_y'\Delta\omega_y' + \frac{\lambda^2\gamma_0 + \alpha_0}{2\alpha_0}\omega_z'\Delta\omega_z'\right], \qquad (11)$$

with C_x, γ_0, and α_0 introduced in Equation (6). In our simulations, we focus on a time window over which $\frac{\mathrm{d}\omega^2}{\mathrm{d}t} = 0$ on average, as shown in Fig. 1. Therefore, in the limiting case of spherical particles, $\lambda = 1$ and $\gamma_0 = \alpha_0 = 2/3$ and $\omega_x'\Delta\omega_x' + \omega_y'\Delta\omega_y' + \omega_z'\Delta\omega_z' = 0$. The rotational work done by the fluid on a particle in one direction in the particle frame is transferred to the other directions. On the other hand, for long fibers (e.g., $\lambda = 50$), one finds $\alpha_0 = 0.9986$ and $\gamma_0 = 0.0029$, and $\omega_x'\Delta\omega_x' + \omega_y'\Delta\omega_y' + 4.11\omega_z'\Delta\omega_z' = \omega_x' S_{yz}' - \omega_y' S_{xz}'$. This shows that the rotational work exerted on the fiber also depends on the fluid velocity gradients around it (embedded in the S_{ij}' terms on the

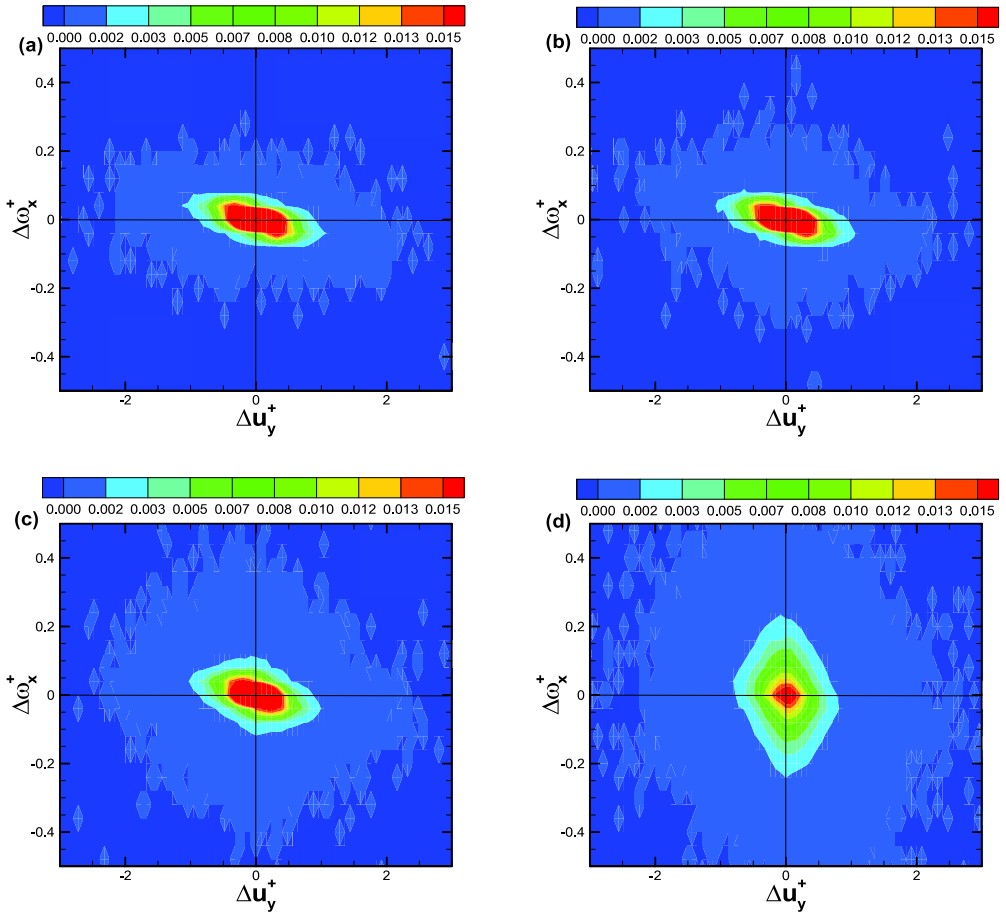

FIG. 12. Effect of fiber elongation on the scatter plots of the instantaneous streamwise slip spin, $\Delta\omega_x^+$, versus spanwise slip velocity, Δu_y^+, conditionally sampled at the $St = 30$ fiber positions. Only fibers in the region $3 \le z^+ \le 7$ are considered. (a) $\lambda = 1$; (b) $\lambda = 3$; (c) $\lambda = 10$; (d) $\lambda = 50$.

right-hand side). In between these two limiting cases and in the absence of two-way coupling, one finds that the rotational energy transferred from the fluid to the fibers depends on the correlation between fiber spin and fluid strain rate, $\omega_i' S_{jk}'$, and on the correlation between fiber spin and slip spin, $\omega_i' \Delta\omega_i'$.

To explore this energy transfer, in Fig. 13, we show the conditionally averaged contributions to the rotational work done by the fluid on the fibers, indicated as $\omega_i' N_i'/C_0$ (with $C_0 = 16\pi\mu a^3\lambda/3$) hereinafter. These contributions were measured in the fiber frame and are considered here to enable a fresh view on fiber-fluid interactions. The rotational work is evaluated considering only fibers with aspect ratio $\lambda = 10$ in the region $7 \le z^+ \le 10$ just outside the viscous sublayer. These statistics are conditioned on the orientation of the fiber with respect to the inertial frame, which is quantified by the orientation angles θ_i already defined in Section IV A. Left-hand side and right-hand side panels in Fig. 13 refer to Stokes numbers $St = 1$ and $St = 30$, respectively.

The values of λ and St examined in Fig. 13 have been chosen to compare the present results with those from earlier studies,[6,31,43,47,49] in which it was demonstrated that relatively long fibers ($\lambda \ge 10$) with modest inertia ($St \le 1$) preferentially align themselves in the streamwise direction near a solid wall, i.e., $\theta_x \simeq 0°$ and $\theta_y \simeq \theta_z \simeq 90°$ (see also Figs. 3 and 4). The left-hand side panels of Fig. 13 show that, for the $St = 1$ fibers, such preferred orientations are associated with the minimum absolute value of all contributions to the fluid-to-fiber rotational energy transfer. When different alignments are attained, the energy transfer is always higher in magnitude, especially

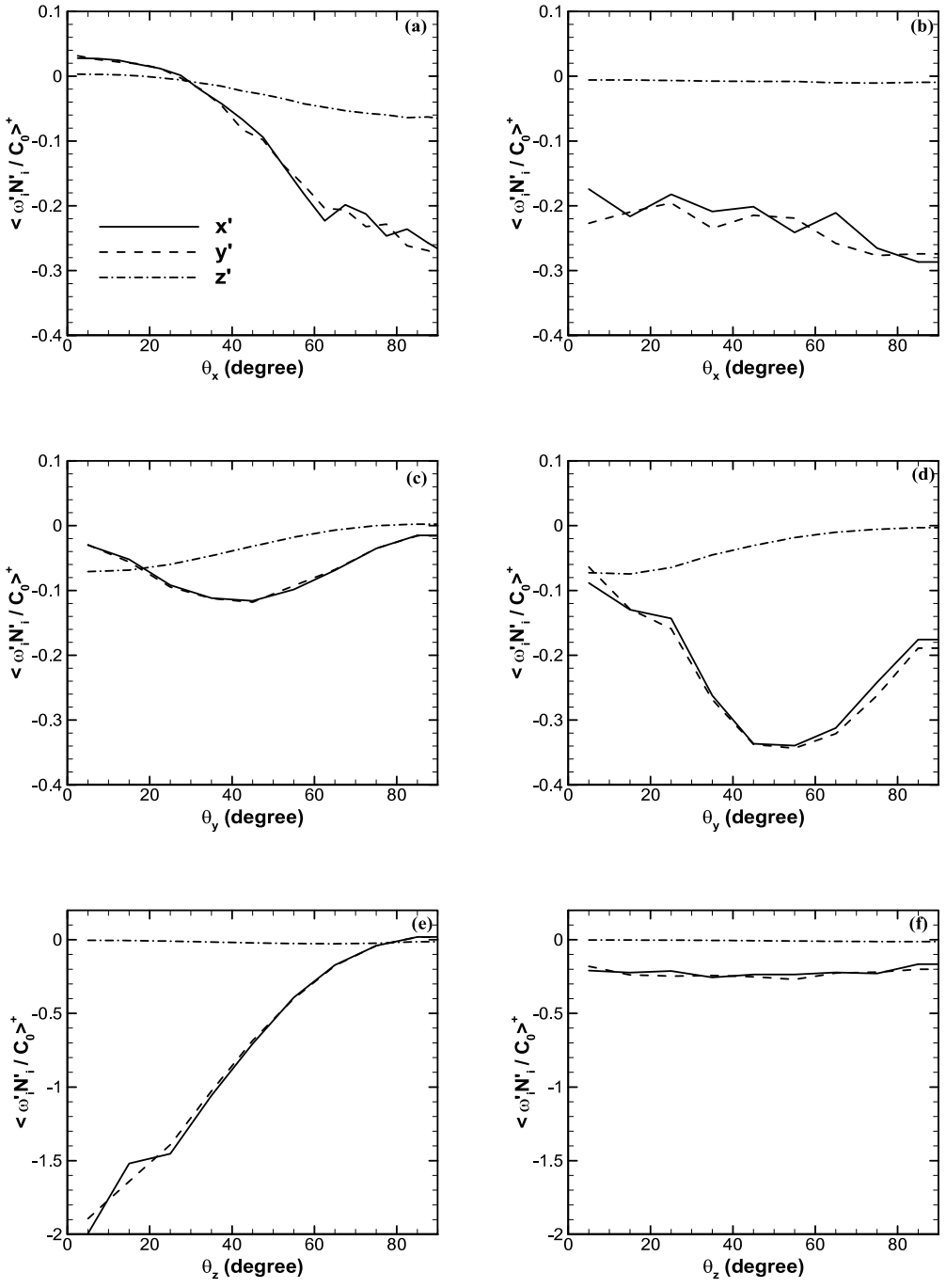

FIG. 13. The rotational work done by the fluid on the $\lambda = 10$ fibers in the fiber frame. The statistics is conditioned to the orientation angle θ_i of a fiber with respect to the x_i-direction in the inertial frame (Fig. 3(a)). Only fibers in the region $7 \le z^+ \le 10$ are considered. Panels (a), (c), and (e): St = 1; panels (b), (d), and (f): St = 30. Lines: solid $\langle \frac{\omega_x' N_x'}{C_0} \rangle$; broken $\langle \frac{\omega_y' N_y'}{C_0} \rangle$; dashed-dotted $\langle \frac{\omega_z' N_z'}{C_0} \rangle$.

when the major symmetry axis z' of the fiber is oriented normal to the wall ($\theta_z \simeq 0°$). It can also be observed that the rotational energy transfer associated with fiber rotation about z', $\langle \frac{\omega_z' N_z'}{C_0} \rangle^+$ (dotted-dashed lines) is generally smaller than that associated with rotation about the two minor axes x' (solid lines) and y' (dashed lines). This is a direct consequence of the lower moment of

inertia and, to a lesser extent, of fiber preferential alignment. Note that because of the axisymmetric shape of the spheroid, rotations about the x' and y' are statistically indistinguishable in all panels and the collapse of the profiles for $\langle \frac{\omega'_x N'_x}{C_0} \rangle^+$ and $\langle \frac{\omega'_y N'_y}{C_0} \rangle^+$ demonstrates the adequacy of the statistical sampling.

If we now examine the right-hand side panels of Fig. 13, we can observe a clear effect of fiber inertia. Profiles for $St = 30$ fibers are generally flatter, indicating that the transferred energy is more modestly dependent on the specific orientation of the fibers, whose preferential alignment with the flow is reduced.[43,47] We also notice that the work done by the fluid on fibers with larger inertia is always negative (Figs. 13(b), 13(d), and 13(f)), suggesting that the fibers tend to lose their rotational energy. This is true also for fibers with smaller inertia, with the exception of those aligned in the streamwise direction ($\theta_x \simeq 0°$, Fig. 13(a)). These fibers tend to receive rotational energy from the fluid through the hydrodynamic torque components N'_x and N'_y. As a final comment, we remark that the rotational work done by the fluid on the fibers is not equal to the work done by the fibers on the fluid. This imbalance is analogous to that between the work done by the drag force on a spherical particle and the work done by this sphere on the surrounding fluid.[56]

V. CONCLUDING REMARKS

In this paper, we have presented a direct numerical simulation based numerical investigation of the rotation of small rigid fibers relative to the surrounding fluid in turbulent channel flow. To simplify the analysis, we focused on one observable. The slip spin, $\Delta\omega_i$, is given by the difference between fluid angular velocity and fiber angular velocity at the fiber center of mass, which allows direct comparison of fiber rotation (and orientation) with the local properties of the carrier flow.

Let us recall that the translational slip velocity recently examined by Zhao *et al.*[25] decreases to zero as the Stokes number goes to zero. This is, however, not the case for the slip spin considered in the present investigation, since the fluid strain rate also contributes to the fiber spin as long as $\lambda > 1$. Challabotla *et al.*[6] studied the shape-dependence of the orientation of non-inertial spheroids and demonstrated that the shape-dependent orientations are carried over to the rotation of the spheroids.

Even if limited to dilute flow conditions, the present results provide new physical insights into the process of fiber rotation in the near-wall region, highlighting in particular how fibers tend to spin relatively to the fluid when entrained in sweep/ejection events. We have demonstrated that this process is strongly intermittent near solid boundaries because small departures from the spherical shape can generate strong fluctuations of $\Delta\omega_i$ and the statistical trends that can be extracted from mean profiles are not representative of the real physics. We have also demonstrated the effect of fiber length on the coupling between the rotational slip velocity vector $\Delta\boldsymbol{\omega}$ and the translational slip velocity vector $\Delta\mathbf{u}$, showing that the two motions become more and more decorrelated as the fiber aspect ratio increases. This is particularly important when one considers the coupling between the spanwise (respectively, streamwise) component of $\Delta\boldsymbol{\omega}$ and the streamwise (respectively, spanwise) component of $\Delta\mathbf{u}$ produced by fiber transport to and away from the wall. Finally, we have examined another aspect of the local interaction between the carrier and dispersed phases: the transfer of rotational energy that occurs from the fluid to the fiber, which we have analyzed based on conditional statistics computed in the fiber frame. By doing so, we can split the work done by the fluid into different contributions that can be associated to different types of rotation for the fiber (referred to as drilling and tumbling in this paper). These statistics show that fibers tend to orient themselves within the flow in order to minimize the transferred rotational energy. Again, it is apparent that this mechanism is strongly affected by fiber length. In more general terms, we observe that fibers with large enough inertia and/or aspect ratio exhibit a stronger resistance to the action of the surrounding turbulence. Because fibers with large translational and rotational inertia do not respond to the behaviour of the fluid flow, all fiber-fluid velocity correlations examined are reduced with increasing inertia or length.

ACKNOWLEDGMENTS

This study has been supported by the Faculty of Engineering Science and Technology (IVT) at NTNU through a research fellowship to L.Z. Computing time was granted by CINECA Supercomputing Center (Bologna, Italy) and by the Research Council of Norway (Programme for Supercomputing). COST Action No. FP1005 is gratefully acknowledged.

[1] M. Kvick, F. Lundell, L. P. Wittberg, and D. Söderberg, "Effect of fibrils on curvature- and rotation-induced hydrodynamic stability," Acta Mech. **224**, 2249-2261 (2013).
[2] F. Lundell, L. D. Söderberg, and P. H. Alfredsson, "Fluid mechanics of papermaking," Annu. Rev. Fluid Mech. **43**, 195-217 (2011).
[3] M. George, R. Elgaddafi, R. Ahmed, and F. Growcock, "Performance of fiber-containing synthetic-based sweep fluids," J. Pet. Sci. Eng. **119**, 185-195 (2014).
[4] P. H. Foss, H. C. Tseng, J. Snawerdt, Y. J. Chang, W. H. Yang, and C. H. Hsu, "Prediction of fiber orientation distribution in injection molded parts using Moldex3D simulation," Polym. Compos. **35**, 671-680 (2014).
[5] R. Ni, S. Kramel, N. Ouellette, and G. A. Voth, "Measurements of the coupling between the tumbling of rods and the velocity gradient tensor in turbulence," J. Fluid Mech. **766**, 202-225 (2015).
[6] N. R. Challabotla, L. Zhao, and H. I. Andersson, "Shape effects on dynamics of inertia-free spheroids in wall turbulence," Phys. Fluids **27**, 061703 (2015).
[7] K. Gustavsson, J. Einarsson, and B. Mehlig, "Tumbling of small axisymmetric particles in random and turbulent flows," Phys. Rev. E **112**, 014501 (2014).
[8] C. Marchioli and A. Soldati, "Rotation statistics of fibers in wall shear turbulence," Acta Mech. **224**, 2311-2330 (2013).
[9] S. Parsa, E. Calzavarini, F. Toschi, and G. A. Voth, "Rotation rate of rods in turbulent fluid flow," Phys. Rev. Lett. **109**, 134501 (2012).
[10] M. Shin and D. L. Koch, "Rotational and translational dispersion of fibers in isotropic turbulent flows," J. Fluid Mech. **540**, 143-173 (2005).
[11] G. G. Marcus, S. Parsa, S. Kramel, N. Rui, and G. A. Voth, "Measurements of the solid-body rotation of anisotropic particles in 3D turbulence," New J. Phys. **16**, 102001 (2014).
[12] L. Chevillard and C. Meneveau, "Orientation dynamics of small, triaxial-ellipsoidal particles in isotropic turbulence," J. Fluid Mech. **737**, 571-596 (2013).
[13] J. Claesson, T. Wikstrom, and A. Rasmuson, "Modeling the effect of fiber orientation on local yield stress in flow of pulp suspensions," Nord. Pulp Pap. Res. J. **29**, 444-452 (2014).
[14] M. Sattari, J. Tuomela, H. Niskanen, and J. Hämäläinen, "Coupled simulation of the spherical angles of rigid fibres by using a fibre orientation probability distribution model," Int. J. Multiphase Flow **65**, 61-67 (2014).
[15] W. Yang, S. H. Shen, and X. K. Ku, "A new model of turbulent fibre suspension and its application in the pipe flow," Can. J. Chem. Eng. **91**, 992-999 (2013).
[16] A. Moosaie, A. Le Duc, and M. Manhart, "A priori analysis of a closure model using the reconstruction of the orientation distribution function in flow of fiber suspensions," Comput. Mech. **48**, 451-459 (2011).
[17] P. Krochak, J. A. Olson, and D. M. Martinez, "Near-wall estimates of the concentration and orientation distribution of a semi-dilute rigid fibre suspension in Poiseuille flow," J. Fluid Mech. **653**, 431-462 (2010).
[18] J. J. J. Gillissen, B. J. Boersma, P. H. Mortensen, and H. I. Andersson, "The stress generated by non-Brownian fibers in turbulent channel flow simulations," Phys. Fluids **19**, 115107 (2007).
[19] J. J. J. Gillissen, B. J. Boersma, P. H. Mortensen, and H. I. Andersson, "On the performance of the moment approximation for the numerical computation of fiber stress in turbulent channel flow," Phys. Fluids **19**, 035102 (2007).
[20] M. Manhart, "Rheology of suspensions of rigid-rod like particles in turbulent channel flow," J. Non-Newtonian Fluid Mech. **112**, 269-293 (2003).
[21] A. Salahuddin, J. Wu, and C. K. Aidun, "Numerical study of rotational diffusion in sheared semidilute fibre suspension," J. Fluid Mech. **692**, 153-182 (2012).
[22] J. A. Olson, "The motion of fibres in turbulent flow, stochastic simulation of isotropic homogeneous turbulence," Int. J. Multiphase Flow **27**, 2083-2103 (2001).
[23] J. A. Olson and R. J. Kerekes, "The motion of fibres in turbulent flow," J. Fluid Mech. **377**, 47-64 (1998).
[24] D. Vincenzi, "Orientation of non-spherical particles in an axisymmetric random flow," J. Fluid Mech. **719**, 465-487 (2013).
[25] L. H. Zhao, C. Marchioli, and H. I. Andersson, "Slip velocity of rigid fibers in turbulent channel flow," Phys. Fluids **26**, 063302 (2014).
[26] A. C. Eringen, "Simple microfluids," Int. J. Eng. Sci. **2**, 205-217 (1964).
[27] A. C. Eringen, "Theory of micropolar fluids," J. Math. Mech. **16**, 1-18 (1966).
[28] H. I. Andersson and L. Zhao, "Bridging the gap between continuum mechanical microrotation viscosity and Lagrangian point-particles," ASME J. Fluids Eng. **135**, 124502 (2013).
[29] M. Byron, J. Einarsson, K. Gustavsson, G. A. Voth, B. Mehlig, and E. Variano, "Shape-dependence of particle rotation in isotropic turbulence," Phys. Fluids **27**, 035101 (2015).
[30] B. G. M. van Wachem, M. Zastawny, F. Zhao, and G. Mallouppas, "Modelling of gas-solid turbulent channel flow with non-spherical particles with large Stokes numbers," Int. J. Multiphase Flow **68**, 80-92 (2015).
[31] A. Abbasi Hoseini, F. Lundell, and H. I. Andersson, "Finite-length effects on dynamical behavior of rod-like particles in wall-bounded turbulent flow," Int. J. Multiphase Flow **76**, 13-21 (2015).
[32] M. Do-Quang, G. A. Amberg, G. B. Brethouwer, and A. V. Johansson, "Simulation of finite-size fibres in turbulent channel flow," Phys. Rev. E **89**, 013006 (2014).
[33] S. Parsa and G. A. Voth, "Inertial range scaling in rotations of long rods in turbulence," Phys. Rev. Lett. **112**, 024501 (2014).

[34] J. Z. Lin, X. Y. Liang, and S. L. Zhang, "Numerical simulation of fiber orientation distribution in round turbulent jet of fiber suspension," Chem. Eng. Res. Des. **90**, 766-775 (2012).
[35] I. Gallily and A. H. Cohen, "On the orderly nature of the motion of nonspherical aerosol particles. II. Inertial collision between a spherical large droplet and axially symmetrical elongated particle," J. Colloid Interface Sci. **68**, 338-356 (1979).
[36] H. Zhang, G. Ahmadi, F. G. Fan, and J. B. McLaughlin, "Ellipsoidal particles transport and deposition in turbulent channel flows," Int. J. Multiphase Flow **27**, 971-1009 (2001).
[37] H. Brenner, "The Stokes resistance of an arbitrary particle IV. Arbitrary fields of flow," Chem. Eng. Sci. **19**, 703-727 (1964).
[38] L. Schiller and A. Z. Naumann, "Über die Grundlegenden Berechnungen bei der Schwerkraftaufbereitung," Z. Ver. Deutsch. Ing. **77**, 318-320 (1933).
[39] C. Kleinstreuer and Y. Feng, "Computational analysis of non-spherical particle transport and deposition in shear flow with application to lung aerosol dynamics—A review," J. Biomech. Eng. **135**, 021008 (2013).
[40] J. Ravnik, C. Marchioli, M. Hribersek, and A. Soldati, "On shear lift force modelling for non-spherical particles in turbulent flows," AIP Conf. Proc. **1558**, 1107 (2013).
[41] G. B. Jeffery, "The motion of ellipsoidal particles immersed in a viscous fluid," Proc. R. Soc. A **102**, 161-179 (1922).
[42] M. Shapiro and M. Goldenberg, "Deposition of glass fiber particles from turbulent air flow in a pipe," J. Aerosol Sci. **24**, 65-87 (1993).
[43] P. H. Mortensen, H. I. Andersson, J. J. J. Gillissen, and B. J. Boersma, "Dynamics of prolate ellipsoidal particles in a turbulent channel flow," Phys. Fluids **20**, 093302 (2008).
[44] P. H. Mortensen, H. I. Andersson, J. J. J. Gillissen, and B. J. Boersma, "On the orientation of ellipsoidal particles in a turbulent shear flow," Int. J. Multiphase Flow **34**, 678-683 (2008).
[45] A. Soldati, M. Casal, P. Andreussi, and S. Banerjee, "Lagrangian simulation of turbulent particle dispersion in electrostatic precipitators," AIChE J. **43**, 1403-1413 (1997).
[46] A. Soldati and C. Marchioli, "Physics and modelling of turbulent particle deposition and entrainment: Review of a systematic study," Int. J. Multiphase Flow **35**, 827-839 (2009).
[47] C. Marchioli, M. Fantoni, and A. Soldati, "Orientation, distribution, and deposition of elongated, inertial fibers in turbulent channel flow," Phys. Fluids **22**, 033301 (2010).
[48] F. Zhao and B. G. M. van Wachem, "Direct numerical simulation of ellipsoidal particles in turbulent channel flow," Acta Mech. **224**, 2331-2358 (2013).
[49] L. H. Zhao, H. I. Andersson, and J. J. J. Gillissen, "On inertial effects of long fibers in wall turbulence: Fiber orientation and fiber stresses," Acta Mech. **224**, 2375-2384 (2013).
[50] C. Marchioli and A. Soldati, "Mechanisms for particle transfer and segregation in turbulent boundary layer," J. Fluid Mech. **468**, 283-315 (2002).
[51] A. Ozolinsa and U. Strautins, "Simple models for wall effect in fiber suspension flows," Math. Modell. Anal. **19**, 75-84 (2014).
[52] H. I. Andersson, L. H. Zhao, and M. Barri, "Torque-coupling and particle-turbulence interactions," J. Fluid Mech. **696**, 319-329 (2012).
[53] L. H. Zhao, C. Marchioli, and H. I. Andersson, "Stokes number effects on particle slip velocity in wall-bounded turbulence and implications for dispersion models," Phys. Fluids **24**, 021705 (2012).
[54] F. Bianco, S. Chibbaro, C. Marchioli, M. V. Salvetti, and A. Soldati, "Intrinsic filtering errors of Lagrangian particle tracking in LES flow fields," Phys. Fluids **24**, 045103 (2012).
[55] P. H. Mortensen, H. I. Andersson, J. J. J. Gillissen, and B. J. Boersma, "Particle spin in a turbulent shear flow," Phys. Fluids **19**, 078109 (2007).
[56] L. H. Zhao, H. I. Andersson, and J. J. J. Gillissen, "Interphasial energy transfer and particle dissipation in particle-laden wall turbulence," J. Fluid Mech. **715**, 32-59 (2013).